

Harvesting Fermionic Field Entanglement in Schwarzschild Spacetime

Nitesh K. Dubey^{a,b}, Sanved Kolekar^{a,b}

^a*Indian Institute of Astrophysics*

Block 2, 100 Feet Road, Koramangala, Bengaluru 560034, India.

^b*Pondicherry University*

R.V.Nagar, Kalapet, Puducherry-605014, India

Email: nitesh.dubey@iiap.res.in, sanved.kolekar@iiap.res.in

21st July 2025

Abstract

We explore entanglement harvesting using two Unruh-DeWitt (UDW) detectors linearly coupled to the scalar density of a massless spin-1/2 field in 1+1 Schwarzschild spacetime. We consider different vacua, including the Boulware, Hartle-Hawking-Israel (HHI), and Unruh vacua, and investigate various configurations of detector trajectories. We find that the transition rate of the static UDW detector exhibits the expected Planckian behavior in the HHI state, while the Unruh state leads to the Helmholtz free energy density of a fermionic thermal bath. We demonstrate that the near-horizon entanglement properties for static detectors in the HHI state have similar behaviour to those in Minkowski vacua for uniformly accelerated detectors in Rindler spacetime. We further consider a different interaction Hamiltonian which breaks local Lorentz symmetry and find that the transition rate of the static detector still exhibits Planckian behavior in the HHI state, while in the Unruh state, it leads to the Helmholtz free energy density of a bosonic or fermionic thermal bath corresponding to the static or conformal 2-bein in interaction, respectively. We observe that the anti-Hawking effect enhances the entanglement between the two detectors while the gravitational redshift and Hawking radiation decrease it. In particular, due to the presence of the anti-Hawking effect, the mutual information and concurrence near the event horizon can be non-zero even for static detectors with static 2-bein, which is in contrast with the case of the scalar field. Conclusions are discussed.

Contents

1	Introduction	3
2	QFT in spherically symmetric spacetime	4
2.1	The classical Schwarzschild spacetime	4
2.2	Dirac field in Schwarzschild spacetime	5
2.3	Different vacua	7
2.3.1	HHI vacuum	7
2.3.2	Unruh state	9
2.3.3	Boulware vacuum	10
2.4	Relative Entanglement entropy of the massless Dirac field	11
3	Introducing Unruh-DeWitt detector formalism	15
3.1	Transition rate	18
3.2	Presence of anti-Hawking effect	19
4	Entanglement harvesting using UDW	21
4.1	Entanglement measures	21
4.2	Vacuum correlations outside the horizon	22
4.2.1	Two static detectors at various separations	22
4.2.2	Keeping the difference of radial coordinate fixed —both detectors are static (SS)	24
4.2.3	Two freely falling detectors (FF)	26
5	Near horizon entanglement of HHI vacuum	29
6	Discussion	32
	Appendices	33
	Appendix A Computing the two point function W_ψ^α	33
	Appendix B Response rate of a static detector in the HHI state	34
	Appendix C Response rate of a static detector in the Unruh state	35
	Appendix D Computing transition probability	36
	Appendix E Monotonicity of $h(x)$ and $g(x)$	36

1 Introduction

The black hole information loss problem has been explored from various perspectives, such as probabilistic spacetime theory, transfinite set theory, quantum metrology, quantum teleportation, relativistic quantum information, the AdS/CFT correspondence, and more [1; 2; 3; 4]. One of the crucial elements in addressing the black hole information loss problem is the quantum entanglement present in matter fields. To have a deeper understanding of the entanglement inherent in the field, one can consider the associated algebra and its properties in the context of a freely chosen tensor-product decomposition of the full state Hilbert space [5]. The Hilbert space decomposition depends upon the reference frames that one chooses. Furthermore, the curvature of spacetime also plays a significant role by affecting the derivatives in field equations that influence the degree of entanglement within the field [6; 7; 8]. The entanglement dynamics of spacetime and matter are particularly important in the framework of an information complete quantum field theory, which may pave a way for unifying quantum theory and general relativity [9; 10]. Additionally, entanglement and other vacuum correlations have also been shown to be affected by other elements, such as the Hawking and local Unruh effect [11; 12; 13; 14]. These effects are also used to explain the transformation between different forms of vacuum correlations [15; 16]. The expected emergence of Hawking particles (or quasi-particles) also carries substantial significance at various other places – apart from black hole physics – in the natural phenomena where quantum excitations propagate within a Lorentzian geometry resembling black holes [17].

In the pursuit of harvesting the entanglement, [18] initially and later [19; 20; 21; 22] proposed a way to harvest the entanglement using quantum probes. In particular, [19] investigated the entanglement present in the vacuum of a massless scalar field by using a pair of causally disconnected two-level detectors coupled to the field. Subsequently, different types of probes were analyzed, including quantum harmonic oscillators and qubits, employing various coupling types, including both linear and nonlinear couplings, in various spacetimes [23; 24; 25; 26; 27; 28; 29; 30; 31]. In particular, [24] and [25] introduce the formalism and limitations of a covariant model of smeared particle detectors. [29] use a complex detector model to study the antiparticle sector of a non-Hermitian field. The distinct entanglement-harvesting profiles due to minimal and conformal couplings have been illustrated in [32]. [33] showed that vacuum entanglement harvesting is significantly more efficient for a smooth switching mechanism than a sudden one, especially for spacelike separations. Moreover, the performance of measurements on quantum fields also affect entanglement harvesting [34].

In the context of black holes, the entanglement harvesting protocol described in [11; 13; 35], involving static detectors coupled to a real massless scalar field, suggests that the horizon inhibits any kind of correlation near it. However, freely falling detectors coupled to the massless scalar field don't experience such decay due to the finite relative gravitational redshift [13]. Furthermore, at near infinite acceleration of the quantum probes, the entanglement of the fermionic field can be either zero or nonzero, unlike that of the scalar field, depending on the choice of the state in the Rindler spacetime as well in the near horizon limit of a Schwarzschild black hole [36; 37]. The generation of entanglement between modes pair of a quantum field within a single, rigid cavity undergoing non-uniform motion in Minkowski space-time is also shown to be influenced by the field's statistics [38]. Moreover, the entanglement tradeoff across horizons also depends on the statistics [39]. The entanglement properties of fermionic fields differ from those of bosonic fields in several contexts. Notably, the manner in which fermionic fields become entangled prompted [40] to suggest that fermionic field entanglement, arising from the expansion of the universe, can be used to reconstruct parameters characterizing the history of cosmic expansion.

Despite the certain different entanglement properties of fermionic and bosonic fields, studies on the entanglement harvesting protocol involving a detector moving along a specified trajectory and coupled to a fermionic field in a black hole spacetime are limited. In particular, the roles of gravitational redshift, the Hawking and anti-Hawking effects, vacuum polarization, and similar phenomena have not been extensively explored for fermionic fields. Takagi [41] initially explored the detector response function of a Unruh DeWitt (UDW) detector coupled linearly to the scalar density of a massless Fermionic field in Minkowski spacetime. Subsequently, [42] and [43] demonstrated the similarities and differences between the UDW coupled linearly to the scalar density of the massless fermionic field and that coupled to a massless scalar field in flat spacetime. Notably, while the numerical values of the entanglement measures, harvested using detectors, depend on various detector parameters — such as the energy gap and the switching function — a systematic comparison can still be made by keeping certain parameters fixed while varying others. [29] studied an example of entanglement harvesting from a fermionic field in flat spacetime. However, the study of entanglement harvesting for fermionic fields in curved spacetime is limited. This further motivates us to compare an analysis of entanglement harvesting for a detector coupled to the scalar density of the Fermionic field with that of a scalar field in the background of a Schwarzschild black hole.

In section 2, we start with a concise review of quantum field theory applied to fermionic fields within the context of curved spacetime and then present the derivation of the two-point functions needed in subsequent sections in various vacuum states. The two-point function in a pure global Gaussian state contains all information about the correlations of

the field. We further briefly review the calculation of the relative entanglement entropy of a massless fermionic field for disjoint intervals in the Schwarzschild spacetime using the two-point function. This yields various interesting properties and inequalities associated with the mutual information of the field in various states. Section 3 introduces the Unruh DeWitt detector (UDW) formalism for fermionic fields and calculates the transition rates of the quantum probe in different vacua, as the transition probability is a competing term in the correlation measures. The transition probability in the usual scenario is positively correlated with temperature; however, it can also decrease with an increase in temperature due to the anti-Hawking effect [44]. We introduce the condition for the anti-Hawking effect and later correlate it with results obtained from entanglement harvesting. Section 4 starts with a discussion of the entanglement measures used in the later subsections. We investigate entanglement harvesting with two static detectors—one in close proximity to the horizon and the other at some proper distance from it. We vary the proper distance between detectors, keeping other parameters constant, and perform entanglement harvesting. The subsequent subsection explores the entanglement characteristics of the vacuum relative to the distance from the horizon, with fixed detector separation and other fixed parameters. The same analysis is also repeated for both detectors in free-fall trajectories in the following subsection. Finally, section 5 provides a comparative analysis of the near-horizon entanglement properties of the Hartle-Hawking state with those of the Minkowski vacua in the context of a uniformly accelerated detector in flat spacetime. Conclusions are discussed in the last section. Use is made of natural units, namely $\hbar=c=k_B=1$, throughout the paper.

2 QFT in spherically symmetric spacetime

We begin with a concise review of quantum field theory applied to fermionic fields within the context of curved spacetime and then present the derivation of the two-point functions in various vacuum states.

We define spacetime as a pair (\mathcal{M}, g) , where \mathcal{M} is a connected 4-dimensional Hausdorff manifold and g is a metric of signature $+2$ on \mathcal{M} [45]. If it admits an isometric action $\Phi : SO(3) \times \mathcal{M} \rightarrow \mathcal{M}$ such that the maximal dimensions of its orbits are two, then we call the spacetime to be spherically symmetric. Any spherically symmetric solution of the vacuum Einstein field equation exhibits local isometry with the Schwarzschild solution [46]. In particular, a non-rotating body undergoing gravitational collapse results in the formation of a Schwarzschild black hole. In this paper, we focus specifically on the Schwarzschild spacetime.

2.1 The classical Schwarzschild spacetime

The Schwarzschild spacetime possesses three globally spacelike Killing vector fields, in addition to one more Killing vector field that is timelike outside the horizon and spacelike inside the horizon. The metric in (1+3) dimensions, using Schwarzschild coordinates, can be expressed as follows:

$$ds^2 = -\left(1 - \frac{2GM}{r}\right)dt_S^2 + \frac{1}{\left(1 - \frac{2GM}{r}\right)}dr^2 + r^2(d\theta^2 + \sin^2\theta d\phi^2). \quad (1)$$

Here M is the ADM mass associated with the geometry, and $\{t_S, r, \theta, \phi\}$ represents the Schwarzschild coordinates. Furthermore, one should also note that the above expression, denoted by Eq.(1), is a classical relation and does not say anything about the quantum states of space-time. However, one can take various matter fields and study their quantum theory in a classical curved spacetime.

For ease of application in later sections, let us introduce null coordinates $v = t_S + r_*$, $u = t_S - r_*$, with $r_* = r + R_s \log |r/R_s - 1|$ and $R_s = 2GM$. Essentially, the constant value of any one of these coordinates describes null geodesics corresponding to ingoing and outgoing directions, respectively. While certain entanglement properties depend upon the angular components, the majority of these properties remain valid when we confine our focus to radial motion exclusively. The truncated Schwarzschild line element, in (1+1) dimensions, in the new coordinates becomes

$$ds^2 = -\frac{R_s}{r}e^{-r/R_s}e^{(v-u)/2R_s}dudv. \quad (2)$$

The above metric, represented as Eq.(2), has a coordinate singularity at $R_s = 2GM$. Nonetheless, it is possible to perform an analytic continuation of this metric, making it regular at all points except for $r=0$. This can be achieved by introducing new coordinates, $U := \mp 2R_s \exp(-u/2R_s)$ and $V := 2R_s \exp(v/2R_s)$, which are commonly referred to as the Kruskal coordinates. The line element corresponding to Kruskal coordinates is

$$ds^2 = -\frac{R_s}{r}e^{-r/R_s}dUdV. \quad (3)$$

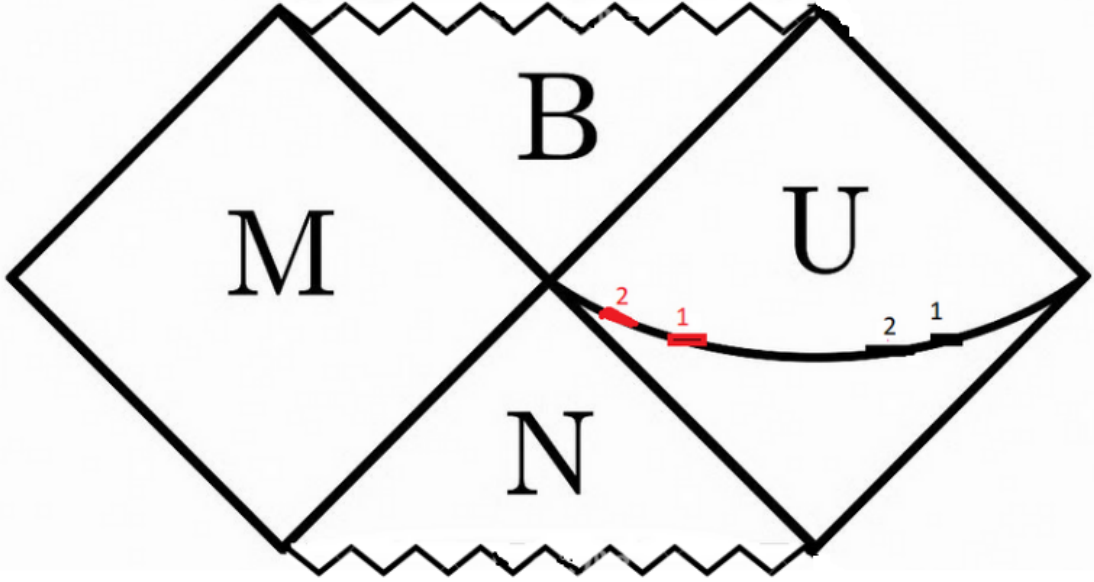


Figure 1: The above plot shows the Penrose diagram for a Schwarzschild black hole. We study the correlation measures of the massless Dirac field in region U. We show four disjoint intervals on a constant Schwarzschild time slice to illustrate the computation of the correlation measures between the red 1 and black 1 intervals, and then between the red 2 and black 2 intervals, corresponding to various distances from the event horizon, while keeping the proper distance between intervals fixed.

In terms of U and v one obtains,

$$ds^2 = -\frac{R_s}{r} e^{-\frac{r}{R_s} + \frac{v}{2R_s}} dU dv. \quad (4)$$

2.2 Dirac field in Schwarzschild spacetime

There may exist a diverse variety of fields on \mathcal{M} that describe the matter content of the spacetime, adhering to either tensorial or spinor equations, and are defined using the metric g on \mathcal{M} . For example, we can have electromagnetic, neutrino, electron, Higgs, or pion field. Metrics other than g or other connections can also be understood as other physical fields. Spinors and spinorial tensor fields arise as realizations of the representation of $\text{ISL}(2, \mathbb{C})$. However, one can define the spinor fields only if the spacetime manifold satisfies certain topological properties [47]. The matter field we consider in the Schwarzschild spacetime is the Dirac spinor, which comprises four components. One can understand it as the combination of an $\text{SL}(2, \mathbb{C})$ spinor and its complex conjugate $\text{SL}(2, \mathbb{C})$ spinor counterpart. The action describing the Dirac field is given by

$$\mathcal{A} = \int d^4x \sqrt{-g(x)} \left\{ \frac{1}{2} i [\bar{\psi} \tilde{\gamma}^\mu \nabla_\mu \psi - (\nabla_\mu \bar{\psi}) \tilde{\gamma}^\mu \psi] - m \bar{\psi} \psi \right\}, \quad (5)$$

where ∇ represents the spinor covariant derivative and $\tilde{\gamma}^\mu$ are the curved space Dirac gamma matrices. One can get the following Dirac equations by varying the above action, denoted by Eq.(5) with respect to $\bar{\psi}$ and ψ , respectively:

$$(i \tilde{\gamma}^\mu \nabla_\mu - m) \psi = 0, \quad (6)$$

$$i \nabla_\mu \bar{\psi} \tilde{\gamma}^\mu + m \bar{\psi} = 0.$$

In n -dimensional spacetime, the above Eqs.(5-6) exhibit conformal invariance in the massless limit as long as $\psi \rightarrow \Omega^{(1-n)/2}(x) \psi$ under conformal transformation of the metric, $g_{\mu\nu}(x) \rightarrow \Omega^2(x) g_{\mu\nu}(x)$. Under the combined local Lorentz and general coordinate transformations on Eq.(5), by imposing the requirement of general covariance of the Dirac equations, Eq.(6), one obtains a condition that is identical to the requirement of covariance under Lorentz transformations in flat spacetime. The key distinction is that in this context, the transformations are local [48] while analyzing quantum entanglement one has to look for nonlocal correlations. Solutions of the Dirac equation form a complete and orthonormal

set of modes that can be quantized by imposing anticommutation relations on the field because quantizing the Dirac field using commutators leads to issues with causality and the energy not being bounded from below [48].

The Schwarzschild metric depends upon the radial coordinate, ‘ r ’, which becomes timelike inside the horizon at $r = R_s = 2GM$. Furthermore, the Schwarzschild spacetime exhibits time-reversal symmetry; however, the quantum state imposed on it need not share the same time-reversal symmetry. However, even with the time dependence of the interior region of the Schwarzschild solution, it is possible to define a globally stable vacuum state [49]. Since the manifold is time-oriented, one can also define the Feynman propagator, which sandwiches time-ordered quantum fields between the state, as follows:

$$iS_{\alpha\beta}^F(x, x') = \langle 0|T(\psi_\alpha(x)\bar{\psi}_\beta(x'))|0\rangle = \theta(t - t')S_{\alpha\beta}^+(x, x') - \theta(t' - t)S_{\alpha\beta}^-(x, x'), \quad (7)$$

where $S_{\alpha\beta}^+$ and $S_{\alpha\beta}^-$ are known as Wightman bi-distributions. The Wightman bi-distributions have a Dirac delta form for null-separated events¹. However, due to relativistic causality, since the Dirac field anticommutes for spacelike-separated events, the time-ordered product does not exhibit any discontinuity when $x_0 = x'_0$. The Feynman propagator for the spin half field satisfies

$$[i\tilde{\gamma}^\mu(x)\nabla_\mu^x - m]S^F(x, x') = [-g(x)]^{-1/2}\delta^n(x - x'). \quad (8)$$

It can be seen by direct substitution that

$$S^F(x, x') = [i\tilde{\gamma}^\mu(x)\nabla_\mu^x + m]G_\phi(x, x'), \quad (9)$$

where $G_\phi(x, x')$ is a bispinor with each component satisfying the Green’s function equation for Klein-Gordon field in curved space-time with a nonminimal coupling [50]. It can be verified using the identity shown in Eq.(3.232) of [48]. In the subsequent sections, we will work with a spacetime that has a zero Ricci scalar, so the Ricci scalar term will be absent. Writing $G_\phi(x, x')$ in terms of scalar Wightman function, $W_\phi(x, x')$, we have [51; 52; 53; 54]

$$iS_{\alpha\beta}^F(x, x') = \theta(t - t')[i\tilde{\gamma}^\mu(x)\nabla_\mu^x + m]U(x, x')W_\phi(x, x')_{\alpha\beta} + \theta(t' - t)[i\tilde{\gamma}^\mu(x)\nabla_\mu^x + m]U(x, x')W_\phi(x', x)_{\alpha\beta}. \quad (10)$$

Here, $U(x, x')$ represents the spinor parallel propagator, which ensures that the above equation, expressed in terms of the scalar field Wightman function, transforms identically to Eq. (7)[52; 53; 54]. Again, relativistic causality ensures that the Feynman propagator (10) is analytic at equal times, and furthermore, the first time derivative is also continuous at equal times. Comparing the above equation, Eq.(10), with Eq.(7), we get the following expressions for the Wightman function of the Dirac field:

$$S_{\alpha\beta}^+(x, x') = [(i\tilde{\gamma}^\mu(x)\nabla_\mu^x + m)U(x, x')W_\phi(x, x')]_{\alpha\beta}, \quad S_{\alpha\beta}^-(x, x') = -[(i\tilde{\gamma}^\mu(x)\nabla_\mu^x + m)U(x, x')W_\phi(x', x)]_{\alpha\beta}. \quad (11)$$

In (1+1)-dimensional Minkowski spacetime, the Wightman function for the Dirac field at two points \tilde{x} and \tilde{x}' on a constant time slice is given by

$$S^+(\tilde{x}, \tilde{x}') = \int \frac{dp}{2\pi} \frac{p_\mu \gamma^\mu + m}{2\sqrt{p^2 + m^2}} \gamma^0 e^{-ip(\tilde{x} - \tilde{x}')}, \quad (12)$$

which evaluates to the following expression in the massless limit: [48; 55; 56; 57]

$$S^+(\tilde{x}, \tilde{x}') = \frac{1}{2}\delta(\tilde{x} - \tilde{x}')\mathbb{1} + \frac{i}{2\pi}\mathcal{P}\left(\frac{1}{\tilde{x} - \tilde{x}'}\right)\gamma^0\gamma^1. \quad (13)$$

Here, $\mathbb{1}$ is the identity matrix, and \mathcal{P} represents that the principal value regularization has been applied. Using the property of conformal invariance, discussed above, we get the following Wightman function for the massless Dirac field in any spacetime which is conformally related to the (1+1) D Minkowski spacetime by a conformal factor Ω [57]:

$$S_{\Omega^2 g}^+(\tilde{x}, \tilde{x}') = \Omega^{-1/2}(\tilde{x})\Omega^{-1/2}(\tilde{x}')\left(\frac{1}{2}\delta(\tilde{x} - \tilde{x}')\mathbb{1} + \frac{i}{2\pi}\mathcal{P}\left(\frac{1}{\tilde{x} - \tilde{x}'}\right)\gamma^0\gamma^1\right). \quad (14)$$

One can also get the above Wightman function, Eq.(14), from Eq.(11) by using $\tilde{\gamma}^\mu = \Omega(x)^{-1}\gamma^\mu$, $U(x, x') = \sqrt{\Omega(x)/\Omega(x')}U_M(x, x')$ where $U_M(x, x')$ is the 1 + 1 Minkowski spinor parallel propagator and $\gamma^\mu\nabla_\mu U(x, x') = 0$.

¹The Wightman bi-distribution gives well-defined results when one integrates over appropriate regions with well-defined boundary conditions. Therefore, we use the term Wightman function in the rest of the paper.

2.3 Different vacua

One usually defines a vacuum state as a Gaussian pure state. The term ‘pure’ means that one cannot decompose the state into a convex combination of other states, and the Gaussian states are states that can be fully described by their one and two-point correlation functions. Generally, it’s not anticipated that the vacuum should be devoid of particles for observers following distinct worldlines. Nevertheless, the symmetries inherent in spacetime dictate the emergence of certain mode sets as natural choices for specific observers. Guided by the principles of normalization and equivalence, one opts for Hadamard states, which are physical states that exhibit a resemblance to the Minkowski vacuum in the high-energy ultraviolet (UV) limit. In a stationary spacetime with a bifurcate Killing horizon, one can identify at most one stationary Hadamard vacuum (see theorem 5.1 of [58]). One can refer [59] for the detailed discussion of states using massless Dirac fields in the Schwarzschild spacetime. For ease of application in the later sections where we use the detectors coupled to the scalar density of the massless fermionic field, this section delves into an exploration of three distinct vacuum states associated with the Schwarzschild spacetime ² and their corresponding two-point functions

$$W_\psi^\alpha(x, x') = \langle 0_\alpha | : \bar{\psi}_a(x) \psi_a(x) :: \bar{\psi}_b(x') \psi_b(x') : | 0_\alpha \rangle \quad (15)$$

$$= -N g^{\mu\rho}(x) \Lambda_\rho^\nu(x', x) \partial_\mu^x W_\phi^\alpha(x, x') \partial_\nu^{x'} W_\phi^\alpha(x, x') \quad (16)$$

Here, $::$ denotes normal ordering, α labels different states, N is the number of spacetime dimensions, Λ_ρ^ν represents the vector parallel transport, and $W_\phi^\alpha(x, x')$ is the Wightman function of a massless scalar field in the corresponding vacuum. The above expression (16) is invariant under general coordinate transformation as well as local Lorentz transformation, and it has been derived in Appendix [A].

The local Lorentz invariance is crucial in defining horizons and the notion of a black hole [60]. It has been suggested in [61] that Lorentz symmetry violations could allow perpetual motion machines of the second kind, and it is proposed that Lorentz symmetry may emerge macroscopically from a microscopic second law of causal horizon thermodynamics. Further, [62] suggests that the violation of Lorentz invariance could allow processes violating the second law of thermodynamics, which is related to the unitarity of the underlying microscopic theory. One can refer [63] for a brief study of fermions in the presence of Lorentz violations. In our case of interaction Hamiltonian giving the two-point function shown in Eq.(16), the Lorentz invariance is preserved due to the presence of the vector parallel propagator Λ_μ^ν . In order to see the effect of violating local Lorentz invariance, with a toy model interaction, we consider a Lorentz symmetry-violating interaction. By defining the decomposition of the spinor parallel propagator as $U(x', x) = \bar{A}(x') A(x)$, $U(x, x') = \bar{A}(x) A(x')$ at every spacetime point, and rescaling the spinor fields as $\psi'(x) = A(x) \psi(x)$, $\bar{\psi}'(x) = \bar{A}(x) \bar{\psi}(x)$, we get an interaction Hamiltonian, along with the following corresponding two-point function computed in Appendix [A]:

$$W_{\psi,b}^{\prime\alpha}(x, x') = \langle 0_\alpha | : \bar{\psi}'_a(x) \psi'_a(x) :: \bar{\psi}'_b(x') \psi'_b(x') : | 0_\alpha \rangle \quad (17)$$

$$= -N b_\delta^{\mu}(x) b_\beta^\nu(x') \eta^{\delta\beta} \partial_\mu^x W_\phi^\alpha(x, x') \partial_\nu^{x'} W_\phi^\alpha(x, x'). \quad (18)$$

The index b represents the choice of the two being taken as the two-point function (18) now depends on the choice of 2-bein $b_\delta^\mu(x)$.

In the rest of the paper, we follow the notation that $W_\psi^\alpha(x, x')$ without the prime is derived from the interaction Hamiltonian \hat{H}_j^{int} in Eq.(61) and is independent of the choice of 2-bein while $W_{\psi,b}^{\prime\alpha}(x, x')$ with the prime is derived from the interaction Hamiltonian $\hat{H}_j^{\prime\text{int}}$ in Eq.(62) and is dependent of the choice of 2-bein.

2.3.1 HHI vacuum

In the eternal Schwarzschild spacetime, there exists exactly one stationary Hadamard vacuum state, which is defined over the entire maximally extended spacetime, known as the Hartle-Hawking-Israel (HHI) state [64]. One understands the left and right exteriors of the event horizon, in this state, to be connected by an Einstein-Rosen bridge, which makes them entangled. To define this state, one quantizes the field using modes in terms of positive frequency with respect to both past and future horizon generators ∂_U and ∂_V . The energy-momentum tensor here has a relatively low magnitude [65], and the geometry closely resembles the classical Schwarzschild solution. Additionally, a static observer far from the event horizon experiences both outgoing and ingoing fluxes of radiation in thermal equilibrium.

The 1+1-dimensional Schwarzschild metric in terms of U and V coordinates (see Eq. (3)) is related to the Minkowski spacetime metric by a conformal factor as $g_{\mu\nu}(x) = \Omega'^2(x) \eta_{\mu\nu}(x)$. Therefore, one can always choose a local orthogonal

²We note that only one is Hadamard over the maximally extended Schwarzschild spacetime. Moreover, uniqueness does not necessarily imply existence in a more general scenario [58].

frame $e_\mu^a(x) = \Omega'(x)\delta_\mu^a$ and compute the spin connection to yield the following vector parallel propagator:

$$\Lambda_\nu^\mu(x, x') = \frac{\Omega'(x')}{\Omega'(x)} \delta_\nu^\mu. \quad (19)$$

Substituting the above expression (19) of the vector parallel propagator in the two-point function of the detector coupled linearly to the scalar density of a massless Dirac field, shown in Eq.(16), with the metric Eq.(3), we get the following two-point function:

$$W_\psi^{\text{HHI}}(x, x') = -\frac{\sqrt{rr'}}{2\pi^2 R_s} e^{(r+r')/2R_s} \frac{1}{(\Delta U - i\epsilon)(\Delta V - i\epsilon)}. \quad (20)$$

Now, using the invariance of Eq. (16) under the local Lorentz transformations and the general coordinate transformations, one can say that Eq. (20) is valid in all reference frames. Since all two-dimensional metrics are related by conformal transformation, imposing the condition of conformal invariance of the action (5) for a massless Dirac field ($m = 0$), for which the field should transform as $\psi \rightarrow \Omega^{(1-n)/2}(x)\psi$ under a conformal transformation of the metric, $g_{\mu\nu}(x) \rightarrow \Omega^2(x)g_{\mu\nu}(x)$, also allows one to get the same two-point function, Eq.(20), using the known two-point function in Minkowski spacetime. One can also get the same expression (20) for the two-point function shown in Eq.(18) by substituting 2-beins³

$$b_0^\mu = \begin{pmatrix} \frac{e^{(v-u)/4R_s}}{\sqrt{1-R_s/r}} \\ \frac{e^{(v-u)/4R_s}}{\sqrt{1-R_s/r}} \end{pmatrix}, \quad b_1^\mu = \begin{pmatrix} \mp \frac{e^{(v-u)/4R_s}}{\sqrt{1-R_s/r}} \\ \pm \frac{e^{(v-u)/4R_s}}{\sqrt{1-R_s/r}} \end{pmatrix}, \quad (21)$$

in Eq.(18).

Since the two-point function shown in Eq. (18) depends on the choice of the 2-bein, we introduce a subscript b , i.e., $W_{\psi,b}^{\text{HHI}}$, to indicate which 2-bein is being used, both here and throughout. So, in this notation, $W_{\psi,c}^{\text{HHI}} = W_\psi^{\text{HHI}}$, where c denotes the conformal tetrad. The timelike component of the 2-bein shown in Eq.(21) represents the four-velocity of a reference frame that is neither freely falling nor static (see Fig 2). Converting the four-velocity in t-r plane by usual tetrad transformation and integrating one gets the following trajectory:

$$\frac{r_*}{2R_s} = -\ln\left(\cosh \frac{t}{2R_s}\right) + C_1, \quad (22)$$

with proper acceleration

$$a := \sqrt{a^\mu a_\mu} = \pm \frac{1 - R_s^2/r^2}{4R_s \sqrt{1 - R_s/r}}, \quad (23)$$

where $r_* = r + R_s \ln|r/R_s - 1|$ is the usual tortoise coordinate and C_1 is an integration constant. For illustration purposes, we show the plots for trajectory and acceleration for a particular C_1 in Fig. 2.

However, the choice of reference frame at any specific point in a curved manifold is entirely arbitrary. One can apply a local, spacetime-dependent Lorentz transformation to Eq.(21) to obtain a 2-bein describing the same geometry but whose zeroth component represents the four-velocity of a desired reference frame. The 2-bein corresponding to a static observer in the metric Eq.(3) is given by:

$$b_0^\mu = \begin{pmatrix} \frac{-U}{2R_s \sqrt{1-R_s/r}} \\ \frac{V}{2R_s \sqrt{1-R_s/r}} \end{pmatrix}, \quad b_1^\mu = \begin{pmatrix} \pm \frac{U}{2R_s \sqrt{1-R_s/r}} \\ \pm \frac{V}{2R_s \sqrt{1-R_s/r}} \end{pmatrix}. \quad (24)$$

The above 2-bein is related to Eq.(21) by just a local Lorentz transformation. Using the 2-bein, Eq.(24), in the Eq.(18), we obtain the following two-point function for the scalar density of the Fermionic field in the HHI vacuum:

$$W_{\psi,s}^{\text{HHI}}(x, x') = \frac{1}{16\pi^2 R_s^2 \sqrt{1-R_s/r} \sqrt{1-R_s/r'}} \frac{V'U + U'V}{(\Delta U - i\epsilon)(\Delta V - i\epsilon)}, \quad (25)$$

where $\Delta U = (U - U')$ and $\Delta V = (V - V')$. The 2-bein moving with a freely falling detector is given by

$$b_0^\mu = \begin{pmatrix} \frac{-U}{2R_s(1-\sqrt{R_s/r})} \\ \frac{V}{2R_s(1+\sqrt{R_s/r})} \end{pmatrix}, \quad b_1^\mu = \begin{pmatrix} \pm \frac{U}{2R_s(1-\sqrt{R_s/r})} \\ \pm \frac{V}{2R_s(1+\sqrt{R_s/r})} \end{pmatrix}, \quad (26)$$

³We refer to the (1+1)-dimensional counterpart of a tetrad as the 2-bein.

which, after substitution in Eq.(18), yields the following two-point function:

$$W'_{\psi,f}{}^{\text{HHI}}(x, x') = \frac{1}{16\pi^2 R_s^2} \left[\frac{UV'}{(1 - \sqrt{R_s/r})(1 + \sqrt{R_s/r'})} + \frac{VU'}{(1 - \sqrt{R_s/r'})(1 + \sqrt{R_s/r})} \right] \frac{1}{(\Delta U - i\epsilon)(\Delta V - i\epsilon)}. \quad (27)$$

2.3.2 Unruh state

In an astrophysical context, black holes are typically formed through the collapse of massive stars, and they do not possess a white hole region. Consequently, astrophysical Schwarzschild black holes do not have radiation coming from infinity. Instead, they only emit outgoing Hawking radiation, leading to a gradual decrease in their mass. Nevertheless, due to their enormously long lifetimes, one can effectively consider the situation to be nearly time-independent. To describe such a scenario, one constructs a state, namely the Unruh state, defined only by the black hole and the universe region, and it reproduces the late-time thermal radiation [66]. Furthermore, the energy density and flux of outgoing radiation far away from the horizon are numerically equal in this state [50]. One can understand the Unruh state as a squeezed state of the initial state that closely resemble the Minkowski vacuum on \mathcal{I}^- . Here, one quantizes the field using positive frequency on the past horizon with respect to the null generator ∂_U of \mathcal{H}^- , and positive frequency modes are derived with respect to the null generators ∂_v on past null infinity.

The 1+1-dimensional Schwarzschild metric in terms of U and v coordinates (see Eq. (4)) is related to the Minkowski spacetime metric by a conformal factor as $g_{\mu\nu}(x) = \Omega'^2(x)\eta_{\mu\nu}(x)$. Therefore, one can always choose a local orthogonal frame $e_\mu^a(x) = \Omega''(x)\delta_\mu^a$ and compute the spin connection to yield the following vector parallel propagator:

$$\Lambda_\nu^\mu(x, x') = \frac{\Omega''(x')}{\Omega''(x)} \delta_\nu^\mu. \quad (28)$$

Substituting the above expression (28) of the vector parallel propagator in the two-point function of the detector coupled linearly to the scalar density of a massless Dirac field, shown in Eq.(16), with the metric Eq.(4), we get the following two-point function:

$$W_\psi^{\text{Unruh}}(x, x') = -\frac{\sqrt{rr'}}{2\pi^2 R_s} e^{(r+r')/2R_s} e^{-(v+v')/4R_s} \frac{1}{(\Delta U - i\epsilon)(\Delta v - i\epsilon)}. \quad (29)$$

Again, one can get the above Eq.(29) by imposing the conformal invariance discussed in subsection 2.3.1, with knowledge of the two-point function in the Minkowski spacetime. This is the same as substituting

$$b_0^\mu = \begin{pmatrix} \frac{e^{-u/4R_s}}{\sqrt{1-R_s/r}} \\ \frac{e^{-u/4R_s}}{\sqrt{1-R_s/r}} \end{pmatrix}, \quad b_1^\mu = \begin{pmatrix} \mp \frac{e^{-u/4R_s}}{\sqrt{1-R_s/r}} \\ \pm \frac{e^{-u/4R_s}}{\sqrt{1-R_s/r}} \end{pmatrix}, \quad (30)$$

in Eq.(18) (i.e, $W'_{\psi,c}{}^{\text{Unruh}} = W_\psi^{\text{Unruh}}$).

Converting the timelike component of the above tetrad (30), which represents the four-velocity of a frame moving with tetrad, in the t - r plane by usual tetrad transformation and integrating, one gets the following trajectory:

$$r_* = -u/2 - R_s e^{-u/2R_s} + C_2 \quad (31)$$

with proper acceleration

$$a := \sqrt{a^\mu a_\mu} = \pm \frac{\cosh(u/4R_s) - 2R_s^2 \cosh(u/4R_s)/r^2 + \sinh(u/4R_s)}{4R_s \sqrt{1-R_s/r}}, \quad (32)$$

where C_2 is an integration constant. For illustrative purposes, we show the plots for the trajectory and acceleration for a particular value of C_2 in Fig. 2.

The 2-bein corresponding to a static observer in the metric Eq.(4) are given by,

$$b_0^\mu = \begin{pmatrix} \frac{-U}{2R_s \sqrt{1-R_s/r}} \\ \frac{1}{\sqrt{1-R_s/r}} \end{pmatrix}, \quad b_1^\mu = \begin{pmatrix} \pm \frac{U}{2R_s \sqrt{1-R_s/r}} \\ \pm \frac{1}{\sqrt{1-R_s/r}} \end{pmatrix}. \quad (33)$$

Using the above 2-bein, Eq. (33), in Eq. (18) yields the two-point function for the scalar density of the Fermionic field in the Unruh vacuum:

$$W'_{\psi,s}{}^{\text{Unruh}}(x, x') = \frac{1}{8\pi^2 R_s \sqrt{1-R_s/r} \sqrt{1-R_s/r'}} \frac{U + U'}{(\Delta U - i\epsilon)(\Delta v - i\epsilon)}, \quad (34)$$

where $\Delta U = (U - U')$ and $\Delta v = (v - v')$. The 2-bein moving with a freely falling detector, expressed in terms of the coordinates used in metric Eq.(4), is given by

$$b_0^\mu = \left(\frac{-U}{\frac{2R_s(1-\sqrt{R_s/r})}{1+\sqrt{R_s/r}}} \right), \quad b_1^\mu = \left(\mp \frac{U}{\frac{2R_s(1-\sqrt{R_s/r})}{1+\sqrt{R_s/r}}} \right), \quad (35)$$

which, after substitution in Eq.(18), yields the following two-point function:

$$W_{\psi,f}'^{\text{Unruh}}(x, x') = \frac{1}{8\pi^2 R_s} \left[\frac{U}{(1-\sqrt{R_s/r})(1+\sqrt{R_s/r'})} + \frac{U'}{(1-\sqrt{R_s/r'})(1+\sqrt{R_s/r})} \right] \frac{1}{(\Delta U - i\epsilon)(\Delta v - i\epsilon)}. \quad (36)$$

2.3.3 Boulware vacuum

The Boulware vacuum corresponds to the vacuum state that replicates the Minkowski vacuum at both past and future null infinity. In other words, in this scenario, there is neither incoming nor outgoing radiation at infinity. Therefore, one can describe the vacuum outside compact, spherically symmetric objects like a static neutron star by Boulware vacuum – given the absence of both past and future event horizons in such objects. It exhibits nonregularity on both past and future horizons. The modes corresponding to this state are defined to be the positive and negative frequency with respect to the Schwarzschild timelike Killing field, denoted as ∂_t .

Again, the 1+1-dimensional Schwarzschild metric in terms of u and v coordinates (see Eq. (2)) is related to the Minkowski spacetime metric by a conformal factor as $g_{\mu\nu}(x) = \Omega''^2(x)\eta_{\mu\nu}(x)$. Therefore, one can again choose a local orthogonal frame $e_\mu^a(x) = \Omega'''(x)\delta_\mu^a$ and compute the spin connection to yield the following vector parallel propagator:

$$\Lambda_\nu^\mu(x, x') = \frac{\Omega'''(x')}{\Omega'''(x)} \delta_\nu^\mu. \quad (37)$$

Substituting the above expression (37) of the vector parallel propagator in the two-point function of the detector coupled linearly to the scalar density of a massless Dirac field, shown in Eq.(16), with the metric Eq.(4), one gets the following two-point function:

$$W_\psi^{\text{Boulware}}(x, x') = -\frac{\sqrt{rr'}}{2\pi^2 R_s} e^{(r+r')/2R_s} e^{-(v+v')/4R_s} e^{(u+u')/4R_s} \frac{1}{(\Delta u - i\epsilon)(\Delta v - i\epsilon)}, \quad (38)$$

which can also be obtained by assuming the conformal invariance discussed in subsection 2.3.1. This is the same as the expression obtained by substituting

$$b_0^\mu = \left(\frac{\frac{1}{\sqrt{1-R_s/r}}}{\frac{1}{\sqrt{1-R_s/r}}} \right), \quad b_1^\mu = \left(\frac{\mp \frac{1}{\sqrt{1-R_s/r}}}{\pm \frac{1}{\sqrt{1-R_s/r}}} \right), \quad (39)$$

in Eq.(18) (i.e, $W_{\psi,c}'^{\text{Boulware}} = W_{\psi,s}'^{\text{Boulware}} = W_\psi^{\text{Boulware}}$). The above 2-bein corresponds to a static frame. The two-point function shown in Eq. (38) can also be rewritten as

$$W_\psi^{\text{Boulware}}(x, x') = W_{\psi,s}'^{\text{Boulware}}(x, x') = -\frac{1}{2\pi^2 \sqrt{1-R_s/r} \sqrt{1-R_s/r'}} \frac{1}{(\Delta u - i\epsilon)(\Delta v - i\epsilon)}, \quad (40)$$

where $\Delta u = (u - u')$ and $\Delta v = (v - v')$. While the 2-bein moving with a freely falling detector in terms of metric Eq.(2) is given by

$$b_0^\mu = \left(\frac{\frac{1}{1-\sqrt{R_s/r}}}{\frac{1}{1+\sqrt{R_s/r}}} \right), \quad b_1^\mu = \left(\frac{\pm \frac{1}{1-\sqrt{R_s/r}}}{\mp \frac{1}{1+\sqrt{R_s/r}}} \right), \quad (41)$$

which, after substitution in Eq.(18), yields the following two-point function

$$W_{\psi,f}'^{\text{Boulware}}(x, x') = -\frac{1}{4\pi^2} \left[\frac{1}{(1-\sqrt{R_s/r})(1+\sqrt{R_s/r'})} + \frac{1}{(1-\sqrt{R_s/r'})(1+\sqrt{R_s/r})} \right] \frac{1}{(\Delta u - i\epsilon)(\Delta v - i\epsilon)}. \quad (42)$$

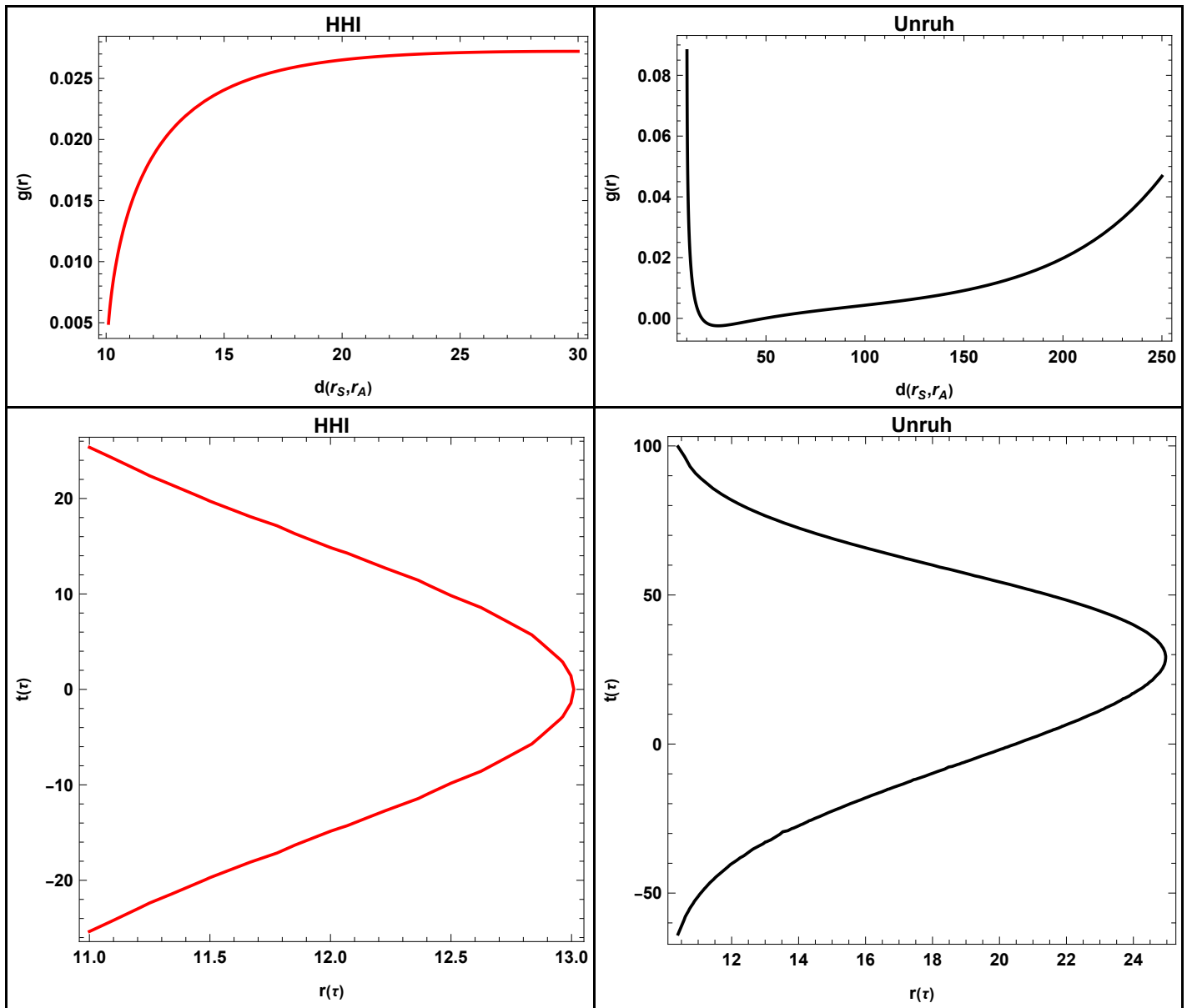


Figure 2: The top panel shows the proper acceleration of a frame where the two-point function for the interaction Hamiltonian \hat{H}_j^{int} shown in Eq. (62) is the same as the two-point function for \hat{H}_j^{int} shown in Eq. (61) i.e, $W_\psi^\alpha = W_{\psi,c}^\alpha$. The bottom panel shows the corresponding trajectory with the integration constants $C_1=1$ and $C_2=78$.

2.4 Relative Entanglement entropy of the massless Dirac field

We briefly review the calculation of the relative entanglement entropy of a massless fermionic field for disjoint intervals in the Schwarzschild spacetime using the two-point function. We shall see that it yields various interesting properties and inequalities associated with the mutual information of the field in various states.

The vacuum states defined in the last section are pure. However, if one considers a restriction to a certain region of spacetime, the reduced state will generally not be pure. The Reeh-Schlieder theorem implies that the reduced state is mixed [67]. From an algebraic point of view, all von Neumann algebras associated with local observables of well-behaved QFTs are isomorphically related. However, algebras associated with local observables in different regions of spacetime can be related in a completely different manner for different QFTs. The entanglement is a kind of quantum correlation between local observables, and it is a property of the algebra of observables. However, observers restricted to certain regions of spacetime and following some specified trajectories can observe different correlations due to their

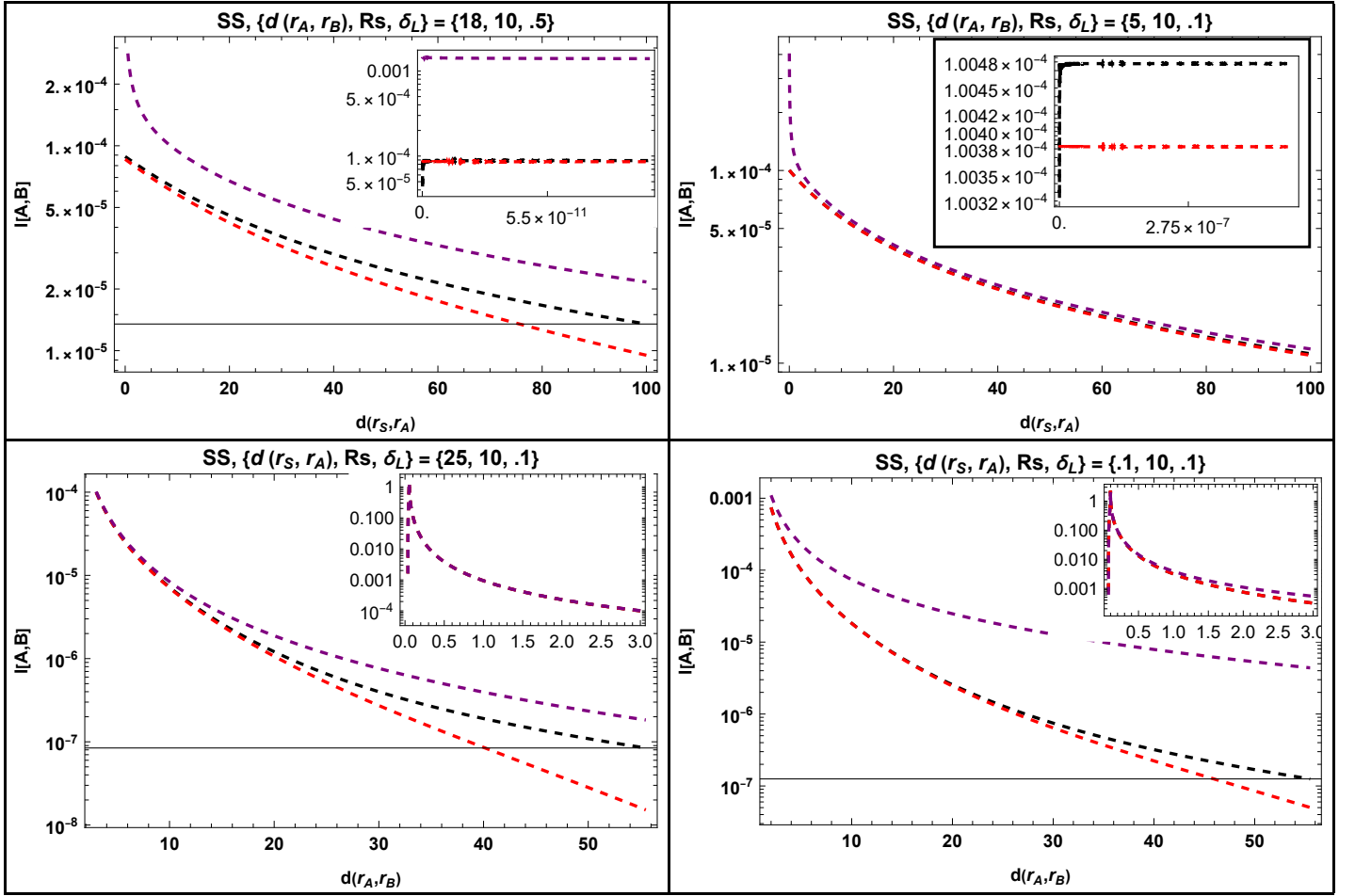


Figure 3: The above plots show the mutual information between two disjoint intervals, $[A, B]$ and $[C, D]$, in a static frame, calculated using the resolvent technique described in Section 2.4. In the plots, the black line represents the Unruh state, the red line represents the Hartle-Hawking-Israel (HHI) state, and the purple line represents the Boulware state. We choose the intervals such that they are at a constant Schwarzschild time slice, and have a spatial extent determined by δ_L . In the top panel, we keep the proper distance between two disjoint intervals, $d(r_A, r_B)$, constant, and vary the distance from the event horizon, $d(r_S, r_A)$. In the bottom panel, we keep the proper distance from the event horizon, $d(r_S, r_A)$, fixed and vary the proper distance between the two disjoint intervals, $d(r_A, r_B)$.

different natural choices of Hilbert space decomposition. In the next section, we will discuss entanglement using localized quantum probes. The entanglement properties studied by the detector depend on several factors, including the choice of detector model. To understand what the quantum probes observe and to compare it with the existing literature on entanglement using various conformal field theory methods, in this section, we first study the relative entanglement entropy — a measure of total correlation — of the field in different states using the resolvent technique [57; 68; 69]. The von Neumann/ entanglement entropy associated with a region having reduced density matrix $\rho_A = \text{Tr}_B |\psi\rangle\langle\psi|$ — which is obtained by tracing out degrees of freedom outside that region — is defined by

$$S_A := -\text{Tr}(\rho_A \log \rho_A). \quad (43)$$

The entanglement entropy of the real massless fermionic field in terms of the Wightman function, Eq.(13), is given by[55]

$$S = -\text{Tr}[(1 - S^+) \log(1 - S^+) + S^+ \log S^+]. \quad (44)$$

Using the integral representation of the logarithm, the above expression can be written as

$$S = - \int_{1/2}^{\infty} d\beta \text{Tr} \left[(\beta - 1/2)(R(\beta) - R(-\beta)) - \frac{2\beta}{\beta + 1/2} \right], \quad (45)$$

where R is the resolvent of the Wightman function, S^+ , and it is given by

$$R = (S^+ - 1/2 + \beta)^{-1}. \quad (46)$$

Using the definition of functional inverse

$$\int d\tilde{z} R(\beta; \tilde{x}, \tilde{z}) R^{-1}(\beta; \tilde{z}, \tilde{y}) = \delta(\tilde{x} - \tilde{y}) \quad (47)$$

we get

$$\int d\tilde{z} R(\beta; \tilde{x}, \tilde{z}) [S^+(\tilde{z}, \tilde{y}) + (\beta - 1/2)\delta(\tilde{z}, \tilde{y})] = \delta(\tilde{x} - \tilde{y}). \quad (48)$$

For the case of massless Dirac field in Minkowski spacetime, the use of the correlator shown in Eq.(13) in the above equation yields

$$\beta R(\tilde{x}, \tilde{y}) - \frac{i}{2\pi} \int \frac{R(\tilde{x}, \tilde{z})}{\tilde{z} - \tilde{y}} d\tilde{z} = \delta(\tilde{x} - \tilde{y}). \quad (49)$$

Assuming the region over which the integration is being performed to have n disjoint spatial intervals, (p_i, q_i) , one gets the following solution of Eq.(49):

$$R(\beta; \tilde{x}, \tilde{y}) = (\beta^2 - 1/4)^{-1} \left(\beta \delta(\tilde{x} - \tilde{y}) + \frac{i\gamma^0 \gamma^1}{2\pi(\tilde{x} - \tilde{y})} \exp \left\{ -\frac{i}{2\pi} \gamma^0 \gamma^1 \log \left(\frac{\beta - 1/2}{\beta + 1/2} \right) (f(\tilde{x}) - f(\tilde{y})) \right\} \right), \quad (50)$$

where

$$f(\tilde{x}) = \log \left(-\frac{\prod_{i=1}^n (\tilde{x}_i - p_i)}{\prod_{i=1}^n (\tilde{x}_i - q_i)} \right). \quad (51)$$

Substituting above resolvent into Eq.(45) and performing integrations with $\tilde{x} \rightarrow \tilde{y}$ [57; 68; 69] one gets

$$S = \frac{1}{3} \left(\sum_{i,j} \log |q_i - p_j| - \sum_{i < j} \log |q_i - q_j| - \sum_{i < j} \log |p_i - p_j| - n \log \epsilon \right). \quad (52)$$

The above expression of entropy is dependent on the UV cutoff ϵ , which appears because of the presence of high-energy vacuum fluctuations. However, assuming ϵ to be a constant, the relative entropy of different regions will be independent of ϵ .

By repeating the above calculation for the correlator Eq.(14) for an interval in a spacetime conformal to (1+1) dimensional Minkowski spacetime, i.e, $g_{\mu\nu} = \Omega^2 \eta_{\mu\nu}$, one gets the following expression of entanglement entropy, in terms of null coordinates (u,v), for a massless Dirac field [70; 71; 72]:

$$S_{[A,B]} = \frac{1}{12} \log \left(\frac{(v_1 - v_2)^2 (u_1 - u_2)^2 \Omega^2(v_1, u_1) \Omega^2(v_2, u_2)}{\epsilon^2} \right), \quad (53)$$

with (u_1, v_1) and (u_2, v_2) being null coordinates of the corners of the interval. The above expression, apart from ϵ , is simply one-third of the natural logarithm of the conformal distance between two corners⁴. Using Eq.(52) again for the two disjoint regions $[A, B]$ and $[C, D]$ one can obtain $S_{[A,B] \cup [C,D]}$. The substitution of the resultant expression along with Eq.(53) in the definition of mutual information

$$I := S_{[A,B]} + S_{[C,D]} - S_{[A,B] \cup [C,D]} \quad (54)$$

we get⁵ [74; 75; 76; 77; 78; 79],

$$I = \frac{1}{12} \log \left(\frac{(v_1 - v_3)^2 (u_1 - u_3)^2 (v_2 - v_4)^2 (u_2 - u_4)^2}{(v_3 - v_2)^2 (u_3 - u_2)^2 (v_1 - v_4)^2 (u_1 - u_4)^2} \right). \quad (55)$$

Here, (u_1, v_1) and (u_2, v_2) are the null coordinates of the corners of the spacelike interval $[A, B]$, and (u_3, v_3) and (u_4, v_4) are those of the spacelike interval $[C, D]$. All corners are ordered by increasing/decreasing spatial coordinates. The above expression of mutual information between two disjoint intervals is Weyl invariant. In particular, it remains invariant under any single transformation or any combination of the following transformations:

⁴The conformal distance transforms covariantly under all conformal isometries of the conformally flat spacetime [73].

⁵This is valid for a massless fermionic field of Dirac type with central charge $c = 1$ in 1+1 dimensions.

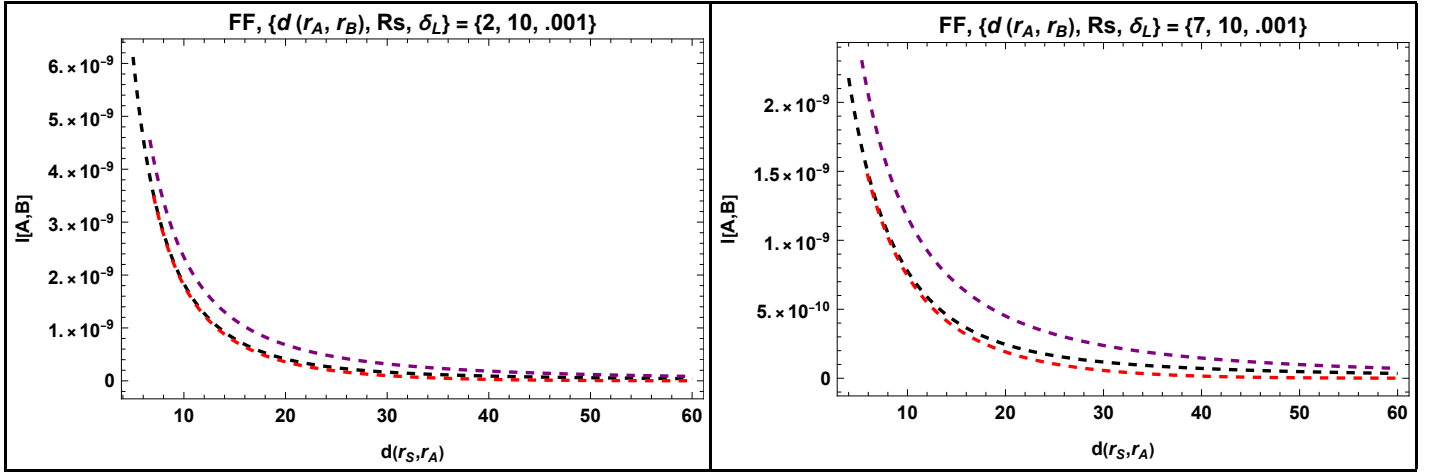


Figure 4: The above plots show the mutual information between two disjoint intervals in a freely falling frame computed using the resolvent technique discussed in section 2.4. In the plots, the black line represents the Unruh state, the red line represents the Hartle-Hawking-Israel (HHI) state, and the purple line represents the Boulware state. We keep the proper distance between two disjoint intervals at a fixed Painleve-Gulstrand time slice constant and vary the distance from the event horizon.

1. $u_1 \rightarrow 1/u_1, u_2 \rightarrow 1/u_2, u_3 \rightarrow 1/u_3, u_4 \rightarrow 1/u_4$
2. $v_1 \rightarrow 1/v_1, v_2 \rightarrow 1/v_2, v_3 \rightarrow 1/v_3, v_4 \rightarrow 1/v_4$
3. $u_1 \rightarrow 1/u_3, u_2 \rightarrow 1/u_4, u_3 \rightarrow 1/u_1, u_4 \rightarrow 1/u_1$
4. $v_1 \rightarrow 1/v_3, v_2 \rightarrow 1/v_4, v_3 \rightarrow 1/v_1, v_4 \rightarrow 1/v_1$
5. $u_1 \rightarrow 1/v_1, u_2 \rightarrow 1/v_2, u_3 \rightarrow 1/v_3, u_4 \rightarrow 1/v_4, v_1 \rightarrow 1/u_1, v_2 \rightarrow 1/u_2, v_3 \rightarrow 1/u_3, v_4 \rightarrow 1/u_4$

One can observe from Eq.(55) that the mutual information I reaches its maximum when the separation between (u_1, v_1) and (u_4, v_4) , or between (u_2, v_2) and (u_3, v_3) , is null. Conversely, it reaches its minimum when the separation between (u_1, v_1) and (u_3, v_3) , or between (u_2, v_2) and (u_4, v_4) , is null. However, since we take the intervals to belong to non-intersecting causal domains, these conditions are not satisfied, leading instead to a finite and nonnegative mutual information⁶. Nevertheless, by keeping both intervals non-intersecting while bringing (u_2, v_2) and (u_3, v_3) close to null, one can observe a peak in the mutual information plots (see Fig.3 and Fig.8). This point acts as a phase transition point of the entanglement. One can refer to [80] for a discussion of the phase transition of the mutual transition by varying the separation between adjacent intervals. Furthermore, the relation of the mutual information with entanglement negativity between adjacent disjoint intervals has been discussed in [81; 82].

The properties of mutual information outlined above are applicable to all three vacua discussed in the previous section. To study different other properties, we first write down the mutual information explicitly. Using Eq.(55), one gets the following expressions of the mutual information for respective vacua :

$$I_{\text{HHI}} = \frac{1}{12} \log \left(\frac{(V_1 - V_3)^2 (U_1 - U_3)^2 (V_2 - V_4)^2 (U_2 - U_4)^2}{(V_3 - V_2)^2 (U_3 - U_2)^2 (V_1 - V_4)^2 (U_1 - U_4)^2} \right), \quad (56)$$

$$I_{\text{Unruh}} = \frac{1}{12} \log \left(\frac{(v_1 - v_3)^2 (U_1 - U_3)^2 (v_2 - v_4)^2 (U_2 - U_4)^2}{(v_3 - v_2)^2 (U_3 - U_2)^2 (v_1 - v_4)^2 (U_1 - U_4)^2} \right), \quad (57)$$

$$I_{\text{Boulware}} = \frac{1}{12} \log \left(\frac{(v_1 - v_3)^2 (u_1 - u_3)^2 (v_2 - v_4)^2 (u_2 - u_4)^2}{(v_3 - v_2)^2 (u_3 - u_2)^2 (v_1 - v_4)^2 (u_1 - u_4)^2} \right). \quad (58)$$

⁶At this point, it is important to recall that the mutual information of a bipartite system is always non-negative. However, the tripartite mutual information of two extended intervals can be negative [76].

We have used Eq. (13) to derive the expression for the entanglement entropy in Eq. (52), which holds on a constant time slice. Therefore, the expressions given in Eqs. (56)–(58) for I_{HHI} , I_{Unruh} , and I_{Boulware} are defined for a constant Schwarzschild time slice. These expressions, can be interpreted by rewriting U and V in terms of \sinh and \cosh , and noting that the Hartle-Hawking-Israel state is thermal in both the outgoing and ingoing modes, while the Unruh state is thermal in the outgoing modes and in the vacuum state for the ingoing modes.

The Kruskal coordinates U and V are given by: $U = -2R_s e^{-u/2R_s}$, $V = 2R_s e^{v/2R_s}$, with $u = t - r_*$, $v = t + r_*$. Let us introduce the dimensionless variables $\eta_s = v_s/2R_s$ and $\xi_s = u_s/2R_s$. The difference between the Boulware and Hartle-Hawking-Israel mutual information is then expressed as

$$I_{\text{Boulware}} - I_{\text{HHI}} = \frac{1}{12} \log \left(\frac{h(\xi_4) g(\eta_4)}{h(\xi_3) g(\eta_3)} \right), \quad (59)$$

where the functions $g(\eta_s)$ and $h(\xi_s)$ are defined in Appendix E. Taking $\xi_1 > \xi_2 > \xi_3 > \xi_4$ (or, $\xi_1 < \xi_2 < \xi_3 < \xi_4$), the monotonicity of the function $h(\xi_s)$, under the assumptions given in Appendix E, implies $h(\xi_4) > h(\xi_3)$. Furthermore, taking $\eta_1 < \eta_2 < \eta_3 < \eta_4$ (or, $\eta_1 > \eta_2 > \eta_3 > \eta_4$), the monotonicity of the function $g(\eta_s)$, under the considerable assumptions in Appendix E, implies $g(\eta_4) > g(\eta_3)$. Therefore, $I_{\text{Boulware}} > I_{\text{HHI}}$. Repeating the procedure outlined above, one can see that

$$I_{\text{Boulware}} > I_{\text{Unruh}} > I_{\text{HHI}} \quad (60)$$

for sufficiently separated regions A and B. For illustration purposes, we show the plots for the mutual information in different vacua from the perspective of a static observer in Fig. 3 and, from the perspective of a freely falling observer in Fig. 4. Therefore, the total correlation between the two disjoint intervals is minimal for the HHI vacuum compared to the other two vacua, while it is maximal for the Boulware vacuum. This difference can be attributed to the presence of Hawking radiation in the HHI and Unruh states, as opposed to only vacuum polarization in the Boulware state. It suggests that the presence of Hawking radiation for a static observer reduces the total correlation. We will defer a detailed analysis of the shapes of the plots in Fig. 3 and Fig. 4 until Section 4, where we will also explore the mutual information derived from entanglement harvesting using detectors.

Having described various vacua and the corresponding entanglement properties, we now proceed to the protocol of entanglement harvesting in the next section.

3 Introducing Unruh-DeWitt detector formalism

Entanglement harvesting is a protocol where one couples certain quantum probes, initially prepared in a joint separable state, to a shared environment. The probes interact locally with the common environment, and after a certain time, we observe that the probes become entangled with each other due to the entanglement inherent in the environment. This protocol can extract the entanglement within the field, even when we do not allow direct communication between the probes [19; 33]. The forecasts made by widely employed particle detectors with spatial smearing, coupled to quantum fields, typically lack general covariance beyond the pointlike limit. The degree of violation of covariance is contingent upon various factors, including the state of the detectors-field system, the configuration and motion status of the detectors, and the characteristics of the spacetime geometry [83]. The absence of covariance becomes evident through an ambiguity in the time-ordering operation. Additionally, the quantum field theories lack well-defined position observables. Nevertheless, the Unruh-DeWitt detector models play a crucial role as a theoretical framework for extracting localized spatiotemporal information from quantum fields. Here, we use a point like Unruh-DeWitt detector (UDW), a two-level system, as a useful theoretical tool for extracting entanglement from the field in Schwarzschild spacetime that admits a Wightman function.

Let the interaction between the field and the j -th detector be governed by the following interaction picture Hamiltonian, which is the closest spinor field equivalent to the scalar field UDWs [41; 42; 43; 84; 85]:

$$\hat{H}_j^{\text{int}}(\tau_j) = \lambda_j \chi_j(\tau_j) \hat{\mu}(\tau_j) : \bar{\psi}(x(\tau_j)) \psi(x(\tau_j)) : . \quad (61)$$

Here τ_j is the proper time in the frame of j^{th} detector, λ_j is a dimensionless coupling constant, $\chi_j(\tau_j)$ represents the switching function and $\hat{\mu}(\tau_j)$ is the monopole coupling of j^{th} detector. Since the Gaussian switching is widely used in the literature on scalar fields [11; 13], we have chosen to employ the same Gaussian switching profile, denoted as $\chi_j(\tau_j) = \exp(-(\tau_j - \tau_{j,0})^2/2\sigma_j^2)$. One can restore the most common form of switching function $\exp(-(\tau_j - \tau_{j,0})^2/\tilde{\sigma}_j^2)$ by rescaling $\sigma \rightarrow \tilde{\sigma}/\sqrt{2}$. Since the Gaussian switching function dies down rapidly, for the sake of numerical simplicity, we do our numerical integrations in the interval $[-5\sigma_j + \tau_{j,0}, 5\sigma_j + \tau_{j,0}]$ [11; 13].

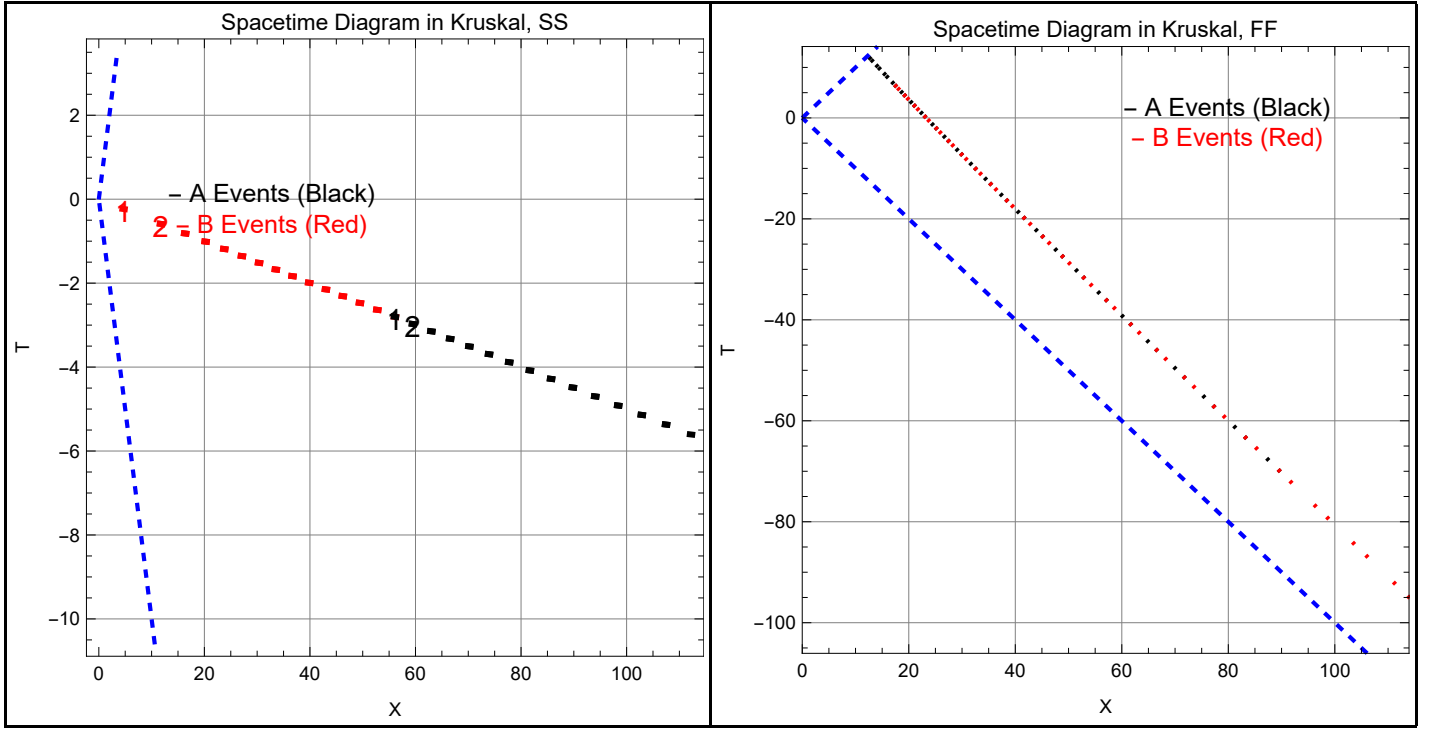


Figure 5: The left panel shows the disjoint intervals for static observers, while the right panel shows those for freely falling observers. The blue dashed lines represent the event horizon. Correlation measures are computed between the disjoint intervals: red 1 with black 1, red 2 with black 2, and so on.

The above monopole coupling shown in Eq.(61) can be viewed as a simplified version of the Hamiltonian describing the coupling of an electron with a photon, which is proportional to $A_\mu \bar{\psi} \gamma^\mu \psi$ [86]. The calculation of two point function in Appendix [A], for the interaction Hamiltonian \hat{H}_j^{int} shown in Eq.(61), involves a spin parallel propagator $U(x, x')$. Since we are working in 1+1 dimensions, the local Lorentz group is abelian and its spinor representation is one-dimensional. So, the spin connection reduces to a single one-form, and we can decompose the spinor parallel propagator as $U(x', x) = \bar{A}(x')A(x)$, $U(x, x') = \bar{A}(x)A(x')$ at every spacetime point. We then define a transformed spinor field as $\psi'(x) = A(x)\psi(x)$, $\bar{\psi}'(x) = \bar{A}(x)\bar{\psi}(x)$. In subsequent subsections, we will also discuss the UDWs coupled to the transformed field with the following interaction Hamiltonian:

$$\hat{H}_j^{\text{int}}(\tau_j) = \lambda_j \chi_j(\tau_j) \hat{\mu}(\tau_j) : \bar{\psi}'(x(\tau_j)) \psi'(x(\tau_j)) : . \quad (62)$$

The spin parallel propagator $U(x, x')$ transforms under a local Lorentz transformation as $U(x, x') \rightarrow D[L(x)] U(x, x') D[L(x')]^{-1}$, where $D[L(x)]$ is the spinor representation of the Lorentz transformation at point x . Factorising $U(x, x') = \bar{A}(x)A(x')$ requires the combination $\bar{A}(x)A(x')$ also to transform as $\bar{A}(x)A(x') \rightarrow D[L(x)] \bar{A}(x)A(x') D[L(x')]^{-1}$. However, individually $A(x')$ and $\bar{A}(x)$ do not transform as $A(x') \rightarrow D[L(x')] A(x') D[L(x')]^{-1}$, $\bar{A}(x) \rightarrow D[L(x)] \bar{A}(x) D[L(x)]^{-1}$ since this does not yield the required transformation property for $U(x, x')$. So, this makes the two-point function $W'_{\psi,b}(x, x')$ shown in Eq. (18), and derived in Appendix A, dependent on the choice of local Lorentz frame through its dependence on the 2-bein.

The following discussions for \hat{H} and \hat{H}' will be similar, so we will not repeat them for both. The time evolution of $\hat{\mu}(\tau_j)$ in the interaction picture, governed by the unperturbed Hamiltonian, is expressed as

$$\hat{\mu}(\tau_j) = \sigma_j^+ e^{i\Omega_j \tau_j} + \sigma_j^- e^{-i\Omega_j \tau_j} . \quad (63)$$

The operators σ^\pm in the above expression represent the SU(2) ladder operators, and Ω_j denotes the energy gap between the detector's ground state $|0\rangle$ and excited state $|1\rangle$. The ladder operators acts as: $\sigma^+ |0\rangle = |1\rangle$, $\sigma^+ |1\rangle = 0$, and $\sigma^- |1\rangle = |0\rangle$, $\sigma^- |0\rangle = 0$. The proper time in the frame of each detector is different. Therefore, we use coordinates based on the proper time of a freely falling test particle from infinity, known as the Painlevé-Gullstrand coordinate system, and

relate all other times to Painlevé-Gullstrand time, denoted as t_{PG} . We set the origin of our Painlevé-Gullstrand time such that the detector starts at rest from infinity at $t_{PG} = -\infty$ and reaches the singularity at $r = 0$ at $t_{PG} = 0$.

The total interaction Hamiltonian for the system of two detectors, A and B, coupled to the background Dirac field, can be written as

$$\hat{H}_{\text{tot}}^{\text{int}}(t_{PG}) = \frac{d\tau_A}{dt_{PG}} \hat{H}_A^{\text{int}}(\tau_A(t_{PG})) \otimes \mathbb{1}_B + \mathbb{1}_A \otimes \frac{d\tau_B}{dt_{PG}} \hat{H}_B^{\text{int}}(\tau_B(t_{PG})). \quad (64)$$

Here \hat{H}_A^{int} and \hat{H}_B^{int} represent interaction Hamiltonians of detectors A and B, respectively and we have employed the fact that both the reparametrized and initial Hamiltonians satisfy the Schrödinger equation, which can be expressed as follows: $\hat{H}(t_{PG})|\psi\rangle = i\frac{d}{dt}|\psi\rangle$ and $\hat{H}(\tau)|\psi\rangle = i\frac{d}{d\tau}|\psi\rangle$. For simplicity, we consider the detectors to be identical; therefore, we have $\Omega_A = \Omega_B = \Omega$. We also assume that both the field and the detector are initially in their respective ground states at the moment when we switch on the detector. Therefore, we can write the initial state as

$$\hat{\rho}_{AB(t_{PG}=0)} = |0_A\rangle\langle 0_A| \otimes |0_B\rangle\langle 0_B| \otimes |0_\alpha\rangle\langle 0_\alpha|. \quad (65)$$

The evolution of the state can be described by the time evolution operator $\hat{U}_I = \mathcal{T}_{t_{PG}} \exp\left(-i \int_{\mathbb{R}} dt_{PG} \hat{H}_{\text{tot}}^{\text{int}}(t_{PG})\right)$, where $\mathcal{T}_{t_{PG}}$ represents the time ordering symbol. Taking the coupling constant λ to be small and tracing over the field degrees of freedom, one obtains the following reduced density matrix in the standard basis (i.e., $|00\rangle, |01\rangle, |10\rangle, |11\rangle$) to the lowest order in λ [19; 13]:

$$\rho_{AB} = \begin{pmatrix} 1 - \mathcal{L}_{AA} - \mathcal{L}_{BB} & 0 & 0 & \mathcal{M}^* \\ 0 & \mathcal{L}_{BB} & \mathcal{L}_{BA} & 0 \\ 0 & \mathcal{L}_{AB} & \mathcal{L}_{AA} & 0 \\ \mathcal{M} & 0 & 0 & 0 \end{pmatrix} + \mathcal{O}(\lambda^4). \quad (66)$$

The matrix elements are specified as follows:

$$\mathcal{L}_{ij} = \lambda^2 \int_{-\infty}^{\infty} d\tau_i \int_{-\infty}^{\infty} d\tau_j' \chi_i(\tau_i) \chi_j(\tau_j') e^{-i\Omega(\tau_i - \tau_j')} W_\psi^\alpha(x_i(\tau_i), x_j(\tau_j')), \quad (67)$$

$$\mathcal{M} = -\lambda^2 \int_{-\infty}^{\infty} d\tau_A \int_{-\infty}^{\infty} d\tau_B \chi_A(\tau_A) \chi_B(\tau_B) e^{i\Omega(\tau_A + \tau_B)} \left[\Theta(t_{PG}(\tau_A) - t_{PG}(\tau_B)) W_\psi^\alpha(x_A(\tau_A), x_B(\tau_B)) + \Theta(t_{PG}(\tau_B) - t_{PG}(\tau_A)) W_\psi^\alpha(x_B(\tau_B), x_A(\tau_A)) \right]. \quad (68)$$

Here, ‘i’ and ‘j’ represent detectors ‘A’ or ‘B,’ $\Theta(\cdot)$ represents the Heaviside step function, and $W_\psi^\alpha(\cdot)$ denotes the pullback of the two-point functions discussed in section 2.3 along the detector’s trajectory. We note that the local contributions, i.e., $i = j$ in Eq.(67), depend on the pullback of the two-point function along the detector trajectory. In contrast, Eq. (68), which governs the nonlocal contribution, depends on the corresponding Feynman propagator, represented by the term in parentheses.

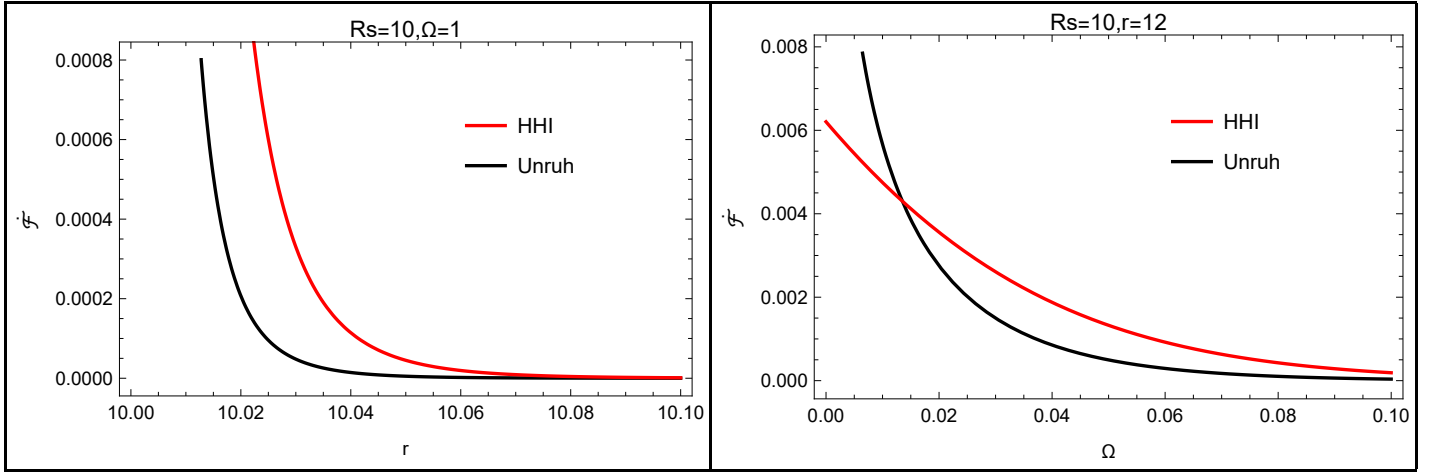


Figure 6: The right plot illustrates the transition rate of a Unruh-DeWitt detector held static in both HHI and Unruh vacua, varying with the energy gap of the detector. Meanwhile, the left plot displays the transition rate as a function of the Schwarzschild radial coordinate.

3.1 Transition rate

As a preliminary to entanglement harvesting, in this subsection, we first analyze the transition rate of the detector for different states.

The elements \mathcal{L}_{AA} and \mathcal{L}_{BB} in the density matrix ρ_{AB} represent the standard expressions for the detector responses of detectors A and B , respectively, along a given trajectory. In contrast, the nonlocal term \mathcal{M} contains the information about entanglement between two detectors. In order to understand what a static detector detects, we define the response rate to linear order in perturbation theory as [50]

$$\dot{\mathcal{F}} = \int_{-\infty}^{\infty} d\Delta\tau e^{-i\Omega\Delta\tau} W_{\psi}^{\alpha}(x(\tau), x(\tau')), \quad (69)$$

where we have switched on the detector smoothly for an infinite time⁷. The above expression is just the Fourier transform of the pullback of the two-point function along the detector's trajectory. For a static detector, due to the timelike Killing symmetry, the two-point functions discussed in section 2.3 depend only on the proper time interval $\Delta\tau = \tau - \tau'$ and the Schwarzschild radial coordinate 'r.' Using the two-point function given in Eq. (40), it can be seen that the transition rate of a static detector with a sufficiently large energy gap, and kept initially in the ground state, in the Boulware vacuum is 0. In contrast, the transition rate of a static detector in the Hartle-Hawking state, for both two-point functions $W_{\psi,s}'^{\text{HHI}}$ defined in (25) and $W_{\psi,c}'^{\text{HHI}} = W_{\psi}^{\text{HHI}}$ defined in (20), is given by

$$\dot{\mathcal{F}}(\Omega) = \frac{\Omega}{\pi(e^{4\pi\kappa R_S\Omega} - 1)} \quad (70)$$

(see Appendix B for detailed calculations), which describes a thermal bath of a bosonic field [42]. The factor π in the above expression would not be present if we express it in terms of frequency rather than angular frequency. It's worth emphasizing that this transition rate for spinor fields in (1+1) dimensions is twice that of Hawking radiation associated with a massless scalar field in (3+1) dimensions, as we are working with a spin-1/2 field [50]. The computation of the transition rate of the static detector in the Unruh vacuum is detailed in Appendix C, and the result is

$$\dot{\mathcal{F}} = \frac{1}{2} \left[2 \times \frac{1}{4\pi^2 R_S \kappa} \log \frac{e^{4\pi\kappa R_S\Omega}}{(e^{4\pi\kappa R_S\Omega} \pm 1)} \right] \quad (71)$$

$$= \frac{1}{4\pi^2 R_S \kappa} \left[\frac{1}{e^{4\pi\kappa R_S\Omega} \pm 1} - \frac{1}{2} \left(\frac{1}{e^{4\pi\kappa R_S\Omega} \pm 1} \right)^2 + \frac{1}{3} \left(\frac{1}{e^{4\pi\kappa R_S\Omega} \pm 1} \right)^3 + \dots \right]. \quad (72)$$

⁷We have dropped a factor that depends only on the structure of the detector.

Here, the plus sign corresponds to the two-point function in the conformal frame tetrad, $W'_{\psi,c}{}^{\text{Unruh}} = W_{\psi}^{\text{Unruh}}$, as given in Eq. (29), while the minus sign corresponds to the two-point function in the static frame tetrad, $W'_{\psi,s}{}^{\text{Unruh}}$, presented in Eq. (34). We write Eq. (71) in this form to remind that there is only an outgoing flux of particles, and we are dealing with the spin-1/2 Dirac field. Remarkably, this is not proportional to the number density of Fermions/Bosons at frequency Ω in a thermal bath. Nevertheless, one can understand it by looking at the Helmholtz free energy of Fermions/Bosons in length L at temperature T [87], which is given by

$$\mathcal{H} = 2L \int_0^\infty \frac{d\Omega}{2\pi} \left[-\Omega + T \log \left(\frac{e^{\Omega/k_B T}}{e^{\Omega/k_B T} \pm 1} \right) \right]. \quad (73)$$

Here, the first term in Eq.(73) represents the zero-point energy. Hence, the transition rate of a static detector far from the black hole in the Unruh state, Eq.(71), is proportional to the Helmholtz free energy density of Fermions/Bosons at a temperature of $1/(4\pi\kappa r_S)$. This contrasts with the findings in [43], where it was observed that the response of UDW for Fermions in Minkowski spacetime with a moving wall boundary exhibits Helmholtz free energy density with Fermionic statistics. Here, the difference in statistics arises from the dependence on $b_\alpha^\mu(x)b_\beta^\nu(x')$ in the two-point functions for different tetrads in the Unruh vacuum. Due to the dependence on $b_\alpha^\mu(x)b_\beta^\nu(x')$ if one doesn't restrict the 2-bein to move with the detector, one would obtain Fermionic statistics using the conformal 2-bein. Thus the nature of the statistics is dependent on the 2-bein chosen. We can further compare the transition rates of a static detector coupled to both types of interaction Hamiltonians, namely, the one associated with the tetrad moving with the detector and the other associated with the conformal symmetry-preserving frame, in both the Unruh state and the HHI state. The corresponding plots are displayed in Fig. 6, which clearly show that the transition rate in both of these vacua decreases as we move away from the horizon. and in the Unruh state, the magnitude for high frequencies is consistently lower than that in the HHI vacuum. However, the transition rate at low frequencies is greater for the Unruh state.

3.2 Presence of anti-Hawking effect

The expressions for the transition rate of the detector in HHI and Unruh states, obtained in Eqs. (70), (71), and further illustrated in Fig. 6, show that the transition rate of a static UDW detector increases as the distance from the horizon decreases. This is consistent with the fact that the KMS temperature for static observers, $T_{KMS} = (64\pi^2 M^2(1 - 2GM/r))^{-1/2}$, also increases with a decrease in r . However, the detector can cool with an increase in temperature, an effect called the anti-Hawking phenomenon [44; 88]. The anti-Hawking phenomenon can be quantified by the negative sign of the partial derivative of transition probability (or the excitation to de-excitation ratio) with respect to KMS temperature. The effective temperature function for the radially infalling observer, with velocity $-\sqrt{2M/r}$ and zero proper acceleration at 'r', is given by [89; 90; 91; 92; 93]

$$T_{\text{eff}} = \frac{1}{1 - \sqrt{R_s/r}} \left(\frac{1}{2R_s} - \frac{R_s}{2r^2} \right), \quad (74)$$

which is the sum of the Hawking and local Unruh components, namely

$$\frac{1}{2R_s(1 - \sqrt{R_s/r})} \quad \text{and} \quad -\frac{R_s}{2r^2(1 - \sqrt{R_s/r})}.$$

The temperature perceived by the observer is given by $T_{\text{eff}}/2\pi$. Therefore, a negative sign of $\partial L_{ii}/\partial T_{\text{eff}}$ should also indicate the weak anti-Hawking effect. Since the transition probability of the detector is a competing term in the entanglement measures, as we shall discuss below in section 4, here, we first investigate the anti-hawking effect in the present subsection.

Substituting the two-point functions corresponding to the static frame tetrad, Eqs.(25) and (34) discussed in the previous section, in Eq.(67) for \mathcal{L}_{ij} and using the saddle point approximation (appendix D) one obtains the following transition probability of a static detector

$$L_{AA,s}^{\text{HHI}} \approx \frac{\lambda^2 \sigma^2}{16\pi R_s^2(1 - R_s/r)} e^{-\Omega^2 \sigma^2} \frac{\cos \frac{\Omega \sigma^2}{R_s \sqrt{(1 - R_s/r)}}}{\sin^2 \left(\frac{\Omega \sigma^2}{2R_s \sqrt{(1 - R_s/r)}} \right)} \quad (75)$$

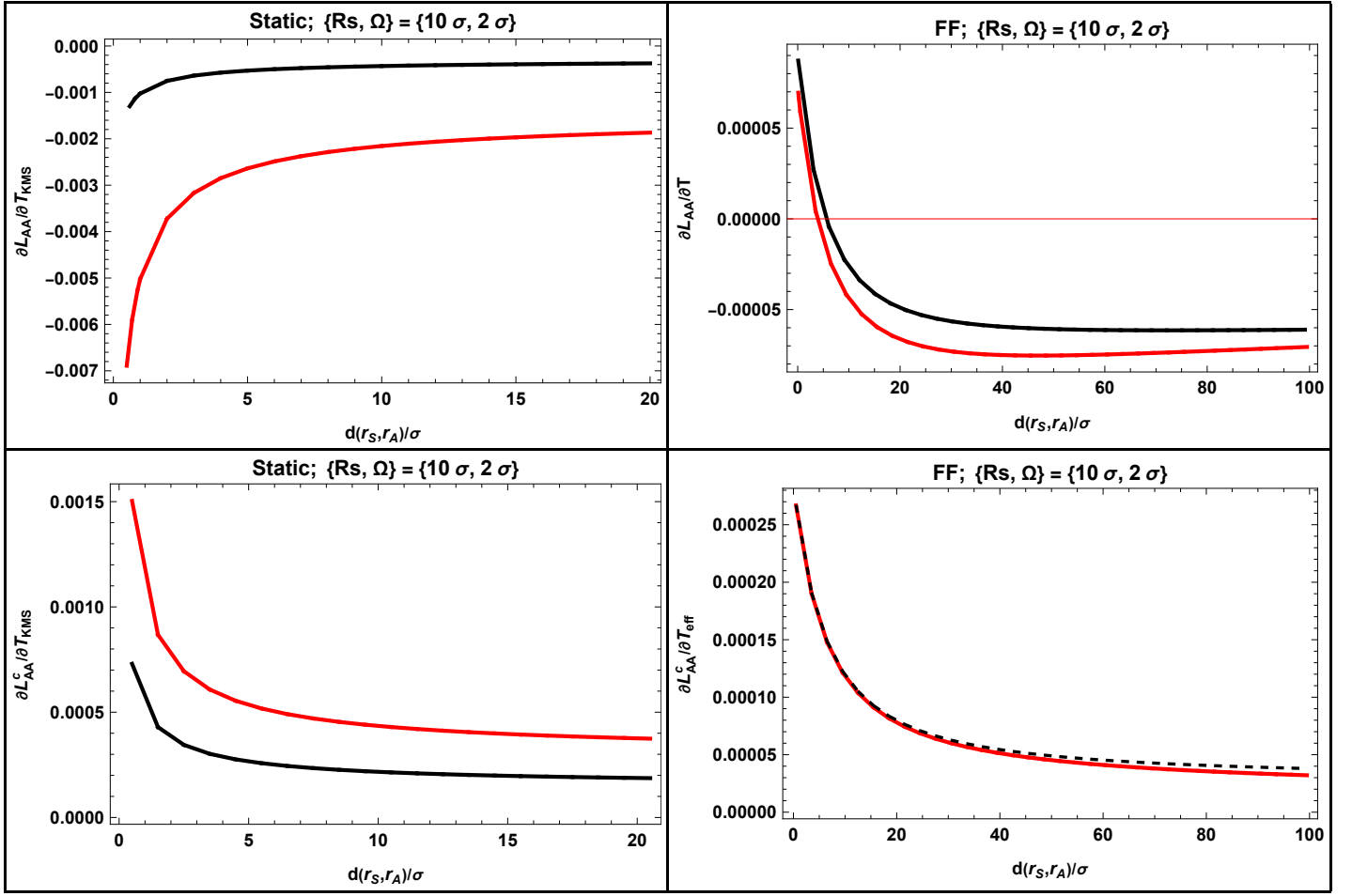


Figure 7: The above figures show the numerical plots of the partial derivative of the transition probability with respect to the KMS temperature as a function of the proper distance from the event horizon on a constant Painleve-Gullstrand time slice (x-axis). In the plots, the black line represents the Unruh state and the red line represents the Hartle-Hawking-Israel (HHI) state. The top panels display the results for the 2-bein co-moving with the detector coupled with the interaction Hamiltonian \hat{H}_j^{int} shown in Eq. (62), while the bottom panels show the results for the interaction Hamiltonian \hat{H}_j^{int} shown in Eq. (61). The UDW in the left panel plots are static while freely falling in the right panels.

and

$$L_{AA,s}^{\text{Unruh}} \approx \frac{\lambda^2}{8\pi R_s \Omega \sqrt{(1 - R_s/r)}} e^{-\Omega^2 \sigma^2} \cot \frac{\Omega \sigma^2}{2R_s \sqrt{(1 - R_s/r)}}. \quad (76)$$

Whereas, the two-point functions corresponding to the conformal symmetry preserving frame tetrad, $W_{\psi,c}'^{\text{HHI}} = W_{\psi}^{\text{HHI}}$ shown in Eq.(20), and $W_{\psi,c}^{\text{Unruh}} = W_{\psi}^{\text{Unruh}}$ shown in Eqs.(29), yield the following transition probability

$$L_{AA,c}^{\text{HHI}} \approx \frac{\lambda^2 \sigma^2}{16\pi R_s^2 (1 - R_s/r)} e^{-\Omega^2 \sigma^2} \text{cosec}^2 \left(\frac{\Omega \sigma^2}{2R_s \sqrt{(1 - R_s/r)}} \right) \quad (77)$$

and

$$L_{AA,c}^{\text{Unruh}} \approx \frac{\lambda^2}{8\pi R_s \Omega \sqrt{(1 - R_s/r)}} e^{-\Omega^2 \sigma^2} \text{cosec} \frac{\Omega \sigma^2}{2R_s \sqrt{(1 - R_s/r)}}. \quad (78)$$

Here, the superscript represents the corresponding state; subscript c stands for conformal, and $\Omega \sigma^2 / 2\kappa R_s < \pi$ has been assumed to make sure that the contribution from the residue term vanishes [94]. Furthermore, we have also assumed the sign of Ω to be positive in the above expressions. In the other case $\Omega < 0$, one would have to shift the contour in

the opposite direction, which will force the contour to cross one pole even in the approximation $\Omega\sigma^2/2\kappa R_s < \pi$, and will bring an exponential factor obeying the detailed balance form of KMS thermality in the case of the HHI state.

The form of Eqs. (75)-(78) for the transition probabilities, apart from a factor of cosine in the numerator, is similar to what has been found in [94] for the scalar field in various cases. From the transition probability expressions (75)-(78), one can further compute $\partial L_{ii}/\partial T_{KMS}$, which determines the presence of the weak anti-Hawking effect. One can also do the same by computing the transition probability integrations numerically without using the saddle point approximation. We compute $\partial L_{ii}/\partial T_{KMS}$ numerically⁸ without using saddle point approximation and plot the graphs in Fig. 7. We find the plots obtained using the numerical integrations and the saddle point approximations in (75)-(78) are consistent with each other⁹. It can be observed from the first plot of Fig. 7 that the derivative of transition probability for a static detector, coupled with two point functions $W_{\psi,s}^{\text{HHI}}$ defined in (25) and $W_{\psi,s}^{\text{Unruh}}$ defined in (34), becomes increasingly negative as one approaches the event horizon. Therefore, the weak anti-Hawking effect for a static detector becomes more prominent as one approaches the event horizon [44; 88]. However, for a freely falling detector (with the two-point functions $W_{\psi,f}^{\text{HHI}}$ and $W_{\psi,f}^{\text{Unruh}}$ defined in (27) and (36)), the top right plot shows that the anti-Hawking is dominant far from the horizon for HHI and Unruh states. In contrast, the bottom left plot of Fig. 7 shows that a static detector with interaction Hamiltonian corresponding to conformal symmetry preserving two-point function $W_{\psi,c}^{\text{HHI}} = W_{\psi}^{\text{HHI}}$ defined in (20) and $W_{\psi,c}^{\text{Unruh}} = W_{\psi}^{\text{Unruh}}$ defined in (29), for the range of parameter space considered throughout the paper, does not encounter any anti-Hawking effect. This property remains valid for a freely falling detector in HHI and Unruh states with $W_{\psi,c}^{\text{HHI}} = W_{\psi}^{\text{HHI}}$ and $W_{\psi,c}^{\text{Unruh}} = W_{\psi}^{\text{Unruh}}$ respectively.

4 Entanglement harvesting using UDW

We discussed above the transition rate and the anti-Hawking effects experienced by the UDW detector. In this section, we introduce the entanglement measure, put two such detectors along a given trajectory, and perform the entanglement harvesting protocol.

4.1 Entanglement measures

For a state ρ_{AB} in the space of states in the Hilbert space of the combined system, an entanglement measure, denoted as $E(\rho_{AB})$, is defined as a mapping from the space of states to the set of non-negative real numbers (\mathbb{R}^+). The entanglement measure must satisfy the following conditions: $E(\rho_{AB}) = 0$ if ρ_{AB} represents a separable state. Additionally, $E(\rho_{AB})$ should not, on average, increase under local operations and classical communications (LOCC). Measuring entanglement is a broad and dynamic area of research in its own right, with many different approaches suggested for quantifying it. The entanglement of formation, intended to assess the resources needed for creating a particular entangled state, is recognized as one of the most fundamental measures [95]. Since the entanglement of formation rises monotonically with the concurrence, determining the concurrence C of the detectors' final state suffices to measure the amount of entanglement between them [95]. It provides a bound on the entanglement. The concurrence is defined by

$$C[\rho_{AB}] := \max[0, \lambda_1 - \lambda_2 - \lambda_3 - \lambda_4], \quad (79)$$

where the λ_s are the square roots of the eigenvalues of $\rho_{AB}\tilde{\rho}_{AB}$ in decreasing order. Here, $\tilde{\rho}_{AB}$ is defined as $(\sigma_y \otimes \sigma_y)\rho_{AB}^*(\sigma_y \otimes \sigma_y)$, and σ_y represents the usual Pauli matrix. Substituting the λ_s for the reduced density matrix ρ_{AB} , shown in (66), in Eq.(79) one obtains [11; 13]

$$C[\rho_{AB}] = 2 \max[0, |\mathcal{M}| - \sqrt{\mathcal{L}_{AA}\mathcal{L}_{BB}}] + \mathcal{O}(\lambda^4). \quad (80)$$

Other forms of quantum correlations, such as quantum discord, which quantifies the overall quantumness of correlations, also play an important role in relativistic quantum information. We also compute the quantum mutual information, which measures the total correlation between two probes. For a quantum bipartite system, it is defined to be the relative entropy between ρ_{AB} and $\rho_A \otimes \rho_B$ [11; 13; 96]

$$I[\rho_{AB}] := S(\rho_{AB}|\rho_A \otimes \rho_B) = S(\rho_A) + S(\rho_B) - S(\rho_{AB}). \quad (81)$$

⁸Here and throughout the paper, we employ the numerical integration techniques described in [11], ensuring stable integration by setting the MinRecursion value to 3 while retaining other parameters at their default settings.

⁹We note that, for the numerical evaluation of the integrals, we truncate the integration limits at 5σ from the peak of the Gaussian switching function. Since the Gaussian switching decays rapidly, this yields results consistent with the Gaussian switching having an infinite tail used in analytical expressions.

Here $S(\cdot)$ denotes the von Neumann entropy, and it is given by the following expressions: $S(\rho_{AB}) = -\text{Tr}_{AB}(\rho_{AB} \log \rho_{AB})$, $S(\rho_A) = -\text{Tr}_A(\rho_A \log \rho_A)$, and $S(\rho_B) = -\text{Tr}_B(\rho_B \log \rho_B)$. By expanding Eq. (81) for mutual information to the leading order in terms of the coupling strength λ , one gets

$$I[\rho_{AB}] = \mathcal{L}_+ \log \mathcal{L}_+ + \mathcal{L}_- \log \mathcal{L}_- - \mathcal{L}_{AA} \log \mathcal{L}_{AA} - \mathcal{L}_{BB} \log \mathcal{L}_{BB} + \mathcal{O}(\lambda^4) \quad (82)$$

where,

$$\mathcal{L}_{\pm} = \frac{1}{2}(\mathcal{L}_{AA} + \mathcal{L}_{BB} \pm \sqrt{(\mathcal{L}_{AA} - \mathcal{L}_{BB})^2 + 4\mathcal{L}_{AB}\mathcal{L}_{BA}}). \quad (83)$$

In the next subsection, we compute the mutual information, and the concurrence for two UDW detectors kept along a given trajectory.

4.2 Vacuum correlations outside the horizon

In the context of a free scalar field in Minkowski spacetime, when we choose to decompose the state space into plane-wave modes, the overall Hilbert space takes the form of a direct product of infinitely countable harmonic oscillator state spaces, each corresponding to a distinct mode k . Consequently, the resultant state appears as a product state rather than an entangled one. However, an alternative approach involves utilizing a tensor product of two-mode squeezed (TMS) states in pairs of Rindler modes, which gives rise to entangled Rindler wedges. Additionally, one can also represent the quantum field's state as a path-ordered or time-ordered exponential operator, acting on local degrees of freedom at each point in space, using variational ansätze like continuous matrix-product states (cMPS) and the continuous multiscale entanglement renormalization ansatz (cMERA) [97; 98]. Such an approach allows for the interpretation of the vacuum state as a multipartite entangled state [99]. There could be multiple possible choices based on the natural choice for the Hilbert space decomposition, which depends upon the reference frame. Hence, the entanglement harvested by the detector is also expected to depend upon trajectory. In this section and the subsequent ones, we delve into the entanglement characteristics of the multipartite entangled state, employing the assistance of two Unruh-DeWitt (UDWs) detectors positioned at distinct locations and following various trajectories.

4.2.1 Two static detectors at various separations

To initiate our investigation, we position two static detectors, labeled A and B, with detector A kept at a radial coordinate of r_A and detector B kept at r_B . Due to their differing radial coordinates, these detectors experience distinct redshift effects. We switch on detector A with the peak of the Gaussian switching function centered at a constant time slice t_{PG} , while the other detector B is activated with its corresponding Gaussian switching function peak delayed by a parameter δ from the constant time slice t_{PG} . The corresponding proper times in terms of t_{PG} and δ are given by

$$\tau_{A0} = \sqrt{1 - \frac{R_s}{r_A}} \left(t_{PG} - 2R_s \sqrt{\frac{r_A}{R_s}} - R_s \log \left| \frac{\sqrt{\frac{r_A}{R_s}} - 1}{\sqrt{\frac{r_A}{R_s}} + 1} \right| \right), \quad (84)$$

$$\tau_{B0} = \delta + \sqrt{1 - \frac{R_s}{r_B}} \left(t_{PG} - 2R_s \sqrt{\frac{r_B}{R_s}} - R_s \log \left| \frac{\sqrt{\frac{r_B}{R_s}} - 1}{\sqrt{\frac{r_B}{R_s}} + 1} \right| \right). \quad (85)$$

The tail of Gaussian switching makes it difficult to arrange both detectors to be purely spacelike separated. However, one can define a communication estimator [13; 100]

$$\mathcal{E} := \frac{\lambda^2}{2} \text{Im} \left(\int_{-\infty}^{+\infty} d\tau_A \int_{-\infty}^{+\infty} d\tau_B \chi(\tau_A) \chi(\tau_B) \langle 0_\alpha | [: \bar{\psi}(x) \psi(x) :, : \bar{\psi}(x') \psi(x') :] | 0_\alpha \rangle \right), \quad (86)$$

whose magnitude broadly characterizes how timelike/spacelike our detectors A and B are. The entanglement harvested by detectors gets contributions both due to the communication as well as due to the intrinsic entanglement present in the field [13; 101]. We choose the constant parameter δ such that the communication estimator, defined in Eq.(86), is minimized. However, taking a very large δ also reduces the magnitude of correlation measures. Hence, we need to optimize a minimum value of δ for which the \mathcal{E} is close to zero. This makes the contribution received due to the communication minimal. We calculate the mutual information and concurrence for this configuration and then repeat the process for various values of the separation between detectors $d(r_A, r_B)$ while keeping R_s and other parameters constant.

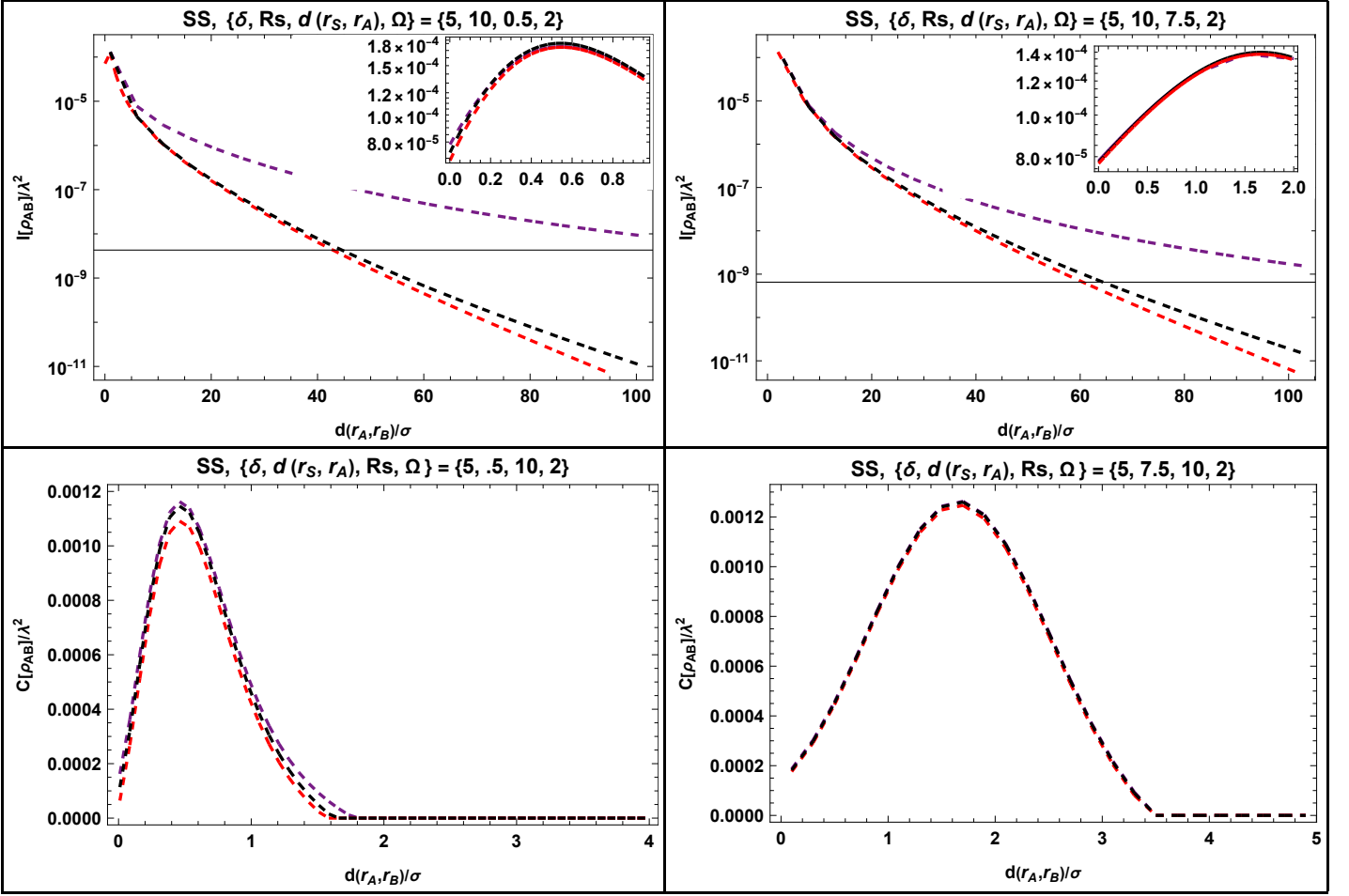


Figure 8: The above figures show the numerical plots of the mutual information (the top panels) and the concurrence (the bottom panels) with two static UDWs as a function of the proper distance between two UDWs on a constant Painleve-Gullstrand time slice (x-axis) while keeping the distance of detector A from the event horizon and all other parameters fixed. In the plots, the black line represents the Unruh state, the red line represents the Hartle-Hawking-Israel (HHI) state, and the purple line represents the Boulware state. Here, the two-point function corresponding to the interaction Hamiltonian shown in Eq.(61), $W_{\psi,c}^{\alpha}$ ($= W_{\psi}^{\alpha}$), is taken.

A static observer at infinity does not experience any flux of radiation in the Boulware vacua. However, at a finite distance from the horizon, due to the curvature of spacetime, the vacuum polarization contributes to the stress-energy tensor [102; 65]. In contrast to the scenario with an infinite switching duration, $\Delta\tau$, or large energy gap Ω where the excitation rate is zero, a static detector in the Boulware vacuum during a finite proper time $\Delta\tau$ experiences transient excitations resulting from the switching process [103]. Therefore, one can also get a nonzero transition rate in the Boulware vacuum. By substituting the pullbacks of the two-point functions W_{ψ}^{HHI} shown in (20), W_{ψ}^{Unruh} shown in (29), and $W_{\psi,s}^{\text{Boulware}}$ ($= W_{\psi}^{\text{Boulware}}$) shown in (38) along the trajectory of a static detector in Eqs. (67), (68) for \mathcal{L}_{ij} and \mathcal{M} , and further using (80), (82) for concurrence and mutual information, we obtain the numerical plots of the correlation measures displayed in Fig. 8, where we have considered the case when one detector is positioned in close proximity to the horizon, and we undertake entanglement harvesting with the second detector held static at various proper separations. Analyzing the results in plots shown in Fig. 8, it is observed that the mutual information, as well as the concurrence in all three vacua, follow the same trend for smaller separation between detectors. One can understand it as all three vacua have similar entanglement properties at small scales. However, for larger separation between detectors, the mutual information as well as the concurrence becomes maximum at a substantial proper separation in the Boulware vacuum state, while it is minimum in the Hartle-Hawking-Israel (HHI) state. The absence of Hawking radiation for a static detector in the Boulware state, coupled with the fact that we are comparing the vacuum correlations of different states

at the same proper distance, where the gravitational redshift, as well as other parameters, remain identical, implies that at sufficiently large distances between detectors, the presence of Hawking radiation in the Unruh and HHI states diminish the total vacuum correlation as well as the entanglement as observed from the vantage point of static detectors¹⁰. As we decrease the proper distance between the UDW detectors, A and B, while keeping detector A fixed near the horizon, the mutual information in all three states increases in such a way that, at smaller separations, all states follow the same trend. Additionally, if detector A is placed at a different radial coordinate, the difference in mutual information between the states—for a given separation between the UDW detectors—changes accordingly. These observations suggest that in the vicinity of the black hole horizon, the energy flux and energy density of Hawking radiation have a detrimental effect on vacuum correlations, causing their degradation.

The observations made in the preceding paragraph, based on UDW formalism, are also consistent with the resolvent technique prediction in section 2.4 (see the bottom panel of Fig. 3). In particular, the relative ordering of mutual information in all three states matches. We noted in section 2.4 (and Fig. 3) that as we decrease the separation between disjoint intervals, there exist specific points where the correlation measure reaches its maximum and then decays again. This feature can also be seen in the entanglement harvesting with UDW in Fig. 8. We observe a peak in the mutual information plots displayed in the bottom panel of Fig. 3. This can be understood as the two disjoint intervals reaching a minimum separation. The standard width of the correlation plots in Fig. 8 increases, indicating a sharper decay near the horizon. This behavior is consistent across all three states, suggesting that these features are primarily due to vacuum polarization and the gravitational redshift effect, as there is no Hawking radiation for a static observer in the Boulware state.

The results in the present subsection indicate that the presence of a horizon has a substantial impact on the vacuum correlations of a quantum field. Nonetheless, we expect other factors, such as the separation distance between detectors, the energy gap, relative velocity, the proper distance from the horizon, and spacetime curvature, to be relevant as well. To examine the dependence of this effect on the distance from the horizon, the following two subsections focus on positioning two Unruh-DeWitt detectors at a fixed separation distance at the time of the peak of switching, denoted as $d(r_A, r_B)$, and explore the entanglement dynamics across various distances from the black hole horizon along various trajectories.

4.2.2 Keeping the difference of radial coordinate fixed —both detectors are static (SS)

In this subsection, we maintain all configurations identical to those in the previous subsection, with the exception that we now vary the distance of detector A from the horizon while keeping the difference in radial coordinates between both detectors, denoted as $d(r_A, r_B)$, fixed at a fixed Painlevé-Gullstrand (PG) time slice. This would correspond to the fixed proper distance between detectors in PG coordinates. The corresponding correlation measures with conformally coupled two-point functions $W_{\psi,c}^{\text{HHI}} (= W_{\psi}^{\text{HHI}})$ defined in (20), $W_{\psi,c}^{\text{Unruh}} (= W_{\psi}^{\text{Unruh}})$ defined in (29), and $W_{\psi,c}^{\text{Boulware}} (= W_{\psi}^{\text{Boulware}})$ defined in (38), as plotted in Fig. 9, exhibit the same relative ordering of correlation measures as in the preceding subsection, as well as in Fig. 3; i.e., the mutual information and the concurrence are maximal for the Boulware state and minimal for the HHI state. This again suggests that the presence of Hawking radiation in HHI and Unruh states diminishes the vacuum correlations. Furthermore, near the event horizon, the correlation measures are close to zero for the HHI and Unruh states, suggesting the gravitational redshift also leads to diminishing the vacuum correlations. In Fig. 10, we have plotted the graphs for concurrence and mutual information for the two-point functions $W_{\psi,s}^{\text{HHI}}$ defined in Eq. (25), $W_{\psi,s}^{\text{Unruh}}$ defined in (34), and $W_{\psi,s}^{\text{Boulware}}$ defined in (40). It can be observed that at any separation scale, the concurrence in all three states demonstrates a similar pattern, which remains nonzero and finite close to the horizon. Moreover, the mutual information is also nonzero near the event horizon for the Unruh and the HHI states. This behavior differs from that observed in the case of scalar fields, as analyzed in [13], where all forms of correlations vanish near the horizon for static detectors in both the Unruh and HHI states. The discussion in the current paragraph suggests that the vanishing of fermionic field entanglement near the horizon depends on the choice of the interaction Hamiltonian. One can choose an interaction Hamiltonian such that the anti-Hawking effect takes place, enhancing entanglement, as opposed to the Hawking effect, which degrades it. One can refer [104], for the state dependence of the decay of the entanglement in the Fermionic field under the infinite acceleration limit, which is the case near the horizon.

It can be seen from the bottom-right and top-right plots of Figs. 9 and 10 that, apart from the decreasing behavior of correlation measures near the horizon, the total correlation, as well as the concurrence, exhibits a local maximum away from the horizon. This behavior is not evident from the top left plot because the mutual information for large-scale separated detectors varies slowly in comparison to the small-scale separated detectors. This contrasts with the bottom

¹⁰Here, one should recall that the Unruh state has only outgoing flux of Hawking radiation, while HHI state has both outgoing as well as ingoing radiation. This explains why the Unruh state correlations are in the middle.

left plot, which shows that the concurrence for large-scale separated detectors decays rapidly and goes to zero as one moves away from the horizon. Near the horizon, both mutual information and concurrence for the Unruh vacuum closely resemble those of the HHI state, while farther from the horizon, these measures align more closely with the Boulware state. The plots in Fig. 10 also suggest that, far from the horizon, the concurrence is minimized for the Boulware state and maximized for the HHI state. However, Fig. 9 show that mutual information and concurrence are minimized for the HHI state and maximized for the Boulware state. This reversal suggests that the anti-Hawking effect, observed for the two-point function used in Fig. 10 (see Fig. 7), enhances entanglement. The HHI state's correlation measures for the case considered in Fig. 10 are maximized due to the dominance of the anti-Hawking effect far from the horizon, whereas for the case of the two point function corresponding to conformal symmetry preserving frame tetrad in Fig. 9, Hawking radiation diminishes correlations in the HHI state.

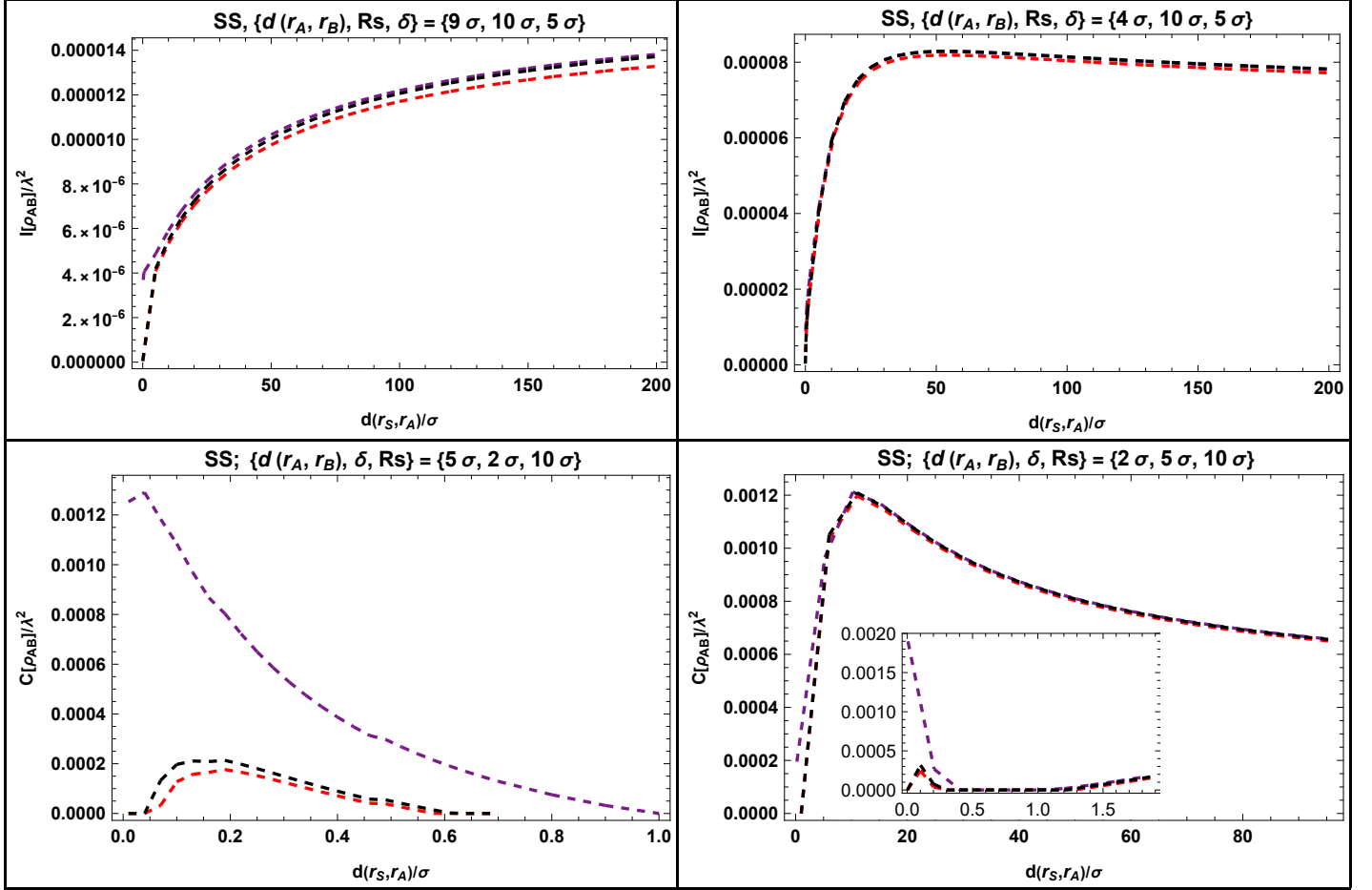


Figure 9: The above figures show the numerical plots of the mutual information (the top panel) and the concurrence (the bottom panel) with two static UDWs as a function of the proper distance of the detector A from the event horizon on a constant Painleve-Gullstrand time slice (x-axis) while keeping the distance between two detectors and all other parameters fixed. In the plots, the black line represents the Unruh state, the red line represents the Hartle-Hawking-Israel (HHI) state, and the purple line represents the Boulware state. Here, the two-point function corresponding to the interaction Hamiltonian shown in Eq.(61), $W'_{\psi,c} (= W_{\psi}^{\alpha})$, is taken. We keep $\Omega = 2\sigma$ in all cases.

One also observes that for smaller separation between detectors, all plots of Fig 9 follow a similar pattern, which is consistent with the observation in the previous subsection 4.2.1 that the entanglement properties on a small scale follow a similar trend in all vacua. Additionally, as the detectors are positioned at greater separations, the concurrence diminishes, especially at larger distances from the horizon. Here, by diminishes, we mean that the concurrence becomes small enough to implement a harvesting protocol with this energy gap. The observations of this section imply that the anti-Hawking effect, in conjunction with Hawking radiation and the gravitational redshift, plays a pivotal role in determining the entanglement properties in the vicinity of a black hole. To explore whether the decay of all correlations

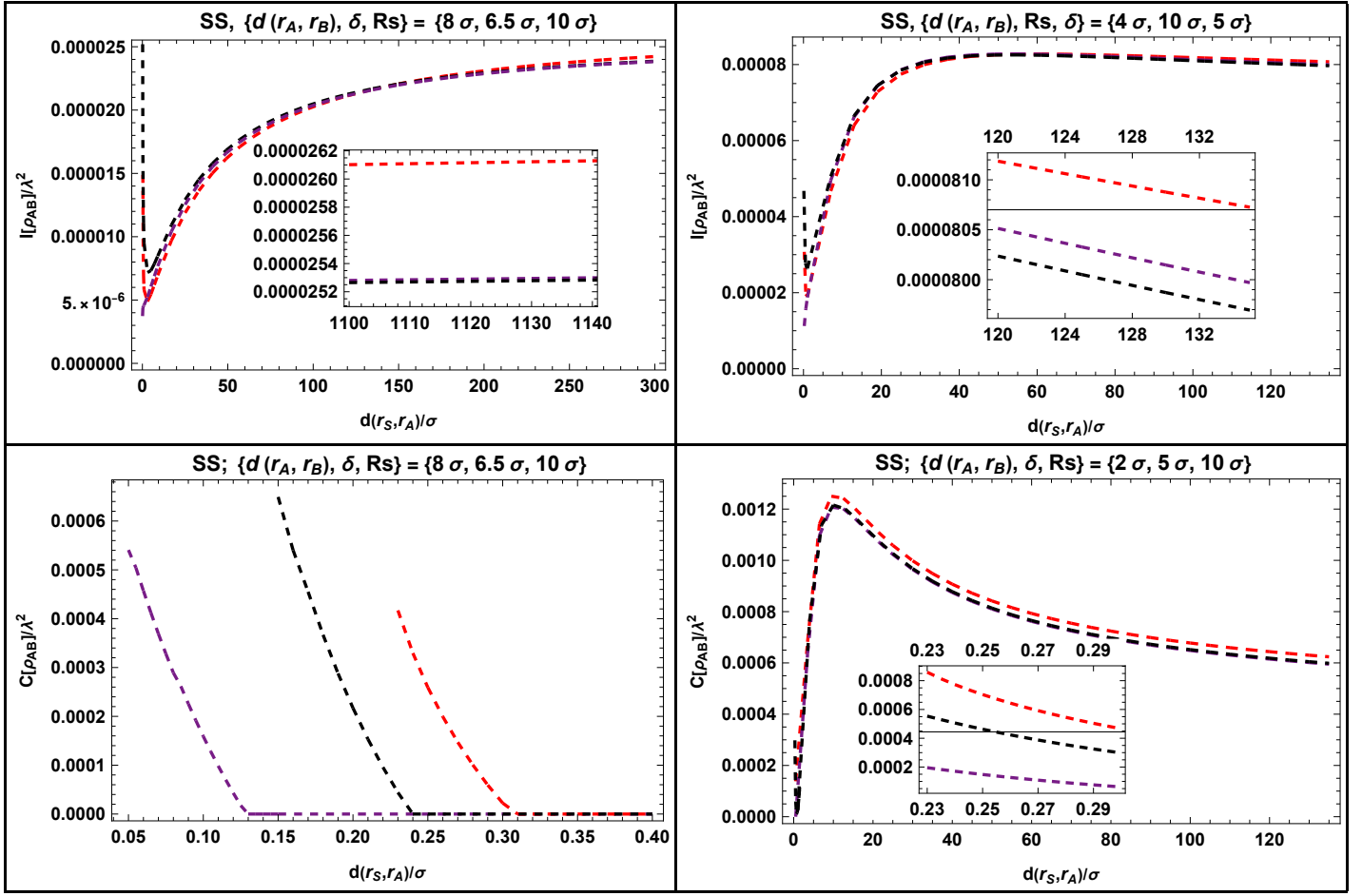


Figure 10: The above figures show the numerical plots of the mutual information (the top panel) and the concurrence (the bottom panel) with two static UDWs, coupled to the field with interaction Hamiltonian \hat{H}_j^{int} , shown in Eq.(62), with static 2-bein, as a function of the proper distance of the detector A from the event horizon on a constant Painleve-Gullstrand time slice (x-axis) while keeping the distance between two detectors and all other parameters fixed. In the plots, the black line represents the Unruh state, the red line represents the Hartle-Hawking-Israel (HHI) state, and the purple line represents the Boulware state. We keep $\Omega = 2\sigma$ in all cases.

in the plots near the horizon is due to the high gravitational redshift and to investigate the role of the anti-Hawking effect further, we consider two freely falling detectors in the next subsection.

4.2.3 Two freely falling detectors (FF)

In the realm of quantum physics, a unique characteristic emerges, where the structure of the Hilbert space can undergo substantial variations among different observers, and the nature of entanglement is contingent upon how one decomposes the state space. The process of black hole evaporation is a physical phenomenon, and, as such, the mass of the black hole must diminish from the perspective of any observer. Consequently, a freely falling timelike detector in the HHI and Unruh states will also perceive the presence of radiation (which need not be thermal) from the black hole [105; 13; 91; 106]. Additionally, a freely falling detector will also perceive a time-dependent vacuum polarization in all three vacua. These facts also motivate us to envisage both detectors as being in free fall from infinity, with Gaussian switching function peaked at different times. We choose detectors to be initially at rest at spatial infinity so that the adapted coordinate system is the Gullstrand-Painlevé coordinates. In this scenario, both the proper distance between the detectors and the gravitational redshift are subject to change over time. Additionally, the local temperature perceived by detectors, defined in Eq.(74), also changes due to the combination of Hawking and anti-Hawking effects.

We consider an ensemble of pairs of radially freely falling detectors and perform entanglement harvesting when the

separation between the two detectors approaches a proper separation $d(r_A, r_B) = r_B - r_A$ (at constant Painleve-Gulstrand time slice), where, r_A and r_B are related to the time of peak τ_{A0} and τ_{B0} of the respective Gaussian switching function, as defined in Eq. (87). The Gaussian switching is centered at the proper times of the individual detectors, given by

$$\tau_{A0} = -\frac{r_A}{3} \sqrt{\frac{4r_A}{R_s}} \quad ; \quad \tau_{B0} = -\frac{r_B}{3} \sqrt{\frac{4r_B}{R_s}} \quad (87)$$

which is precisely the time taken by a freely falling test particle to arrive at r_A or r_B , respectively, starting from infinity with zero initial velocity. The entanglement harvesting is repeated with this setup multiple times, varying the distance of the switching function peak of the nearest detector from the horizon, while keeping $d(r_A, r_B)$ same for all pairs. The results are shown in Figs. 11 and 12.

It's worth noting that in the case of the Boulware vacuum, we refrain from conducting measurements very close to the horizon, as the freely falling detector must inevitably cross the horizon, and the state is not well-defined in that region. Hence, we can compare entanglement measures at locations far away from the horizon for the Boulware vacuum.

We have employed a pointlike detector, which means that in the case of free fall, it does not locally experience any gravitational field. This characteristic allows us to collect entanglement data very near the black hole horizon. Furthermore, in the reference frame of the freely falling detector, the effective temperature, defined in Eq.(74), at the horizon remains finite [91], as the observer in this frame is not subjected to acceleration locally. Therefore, we do not expect the correlations to decay near the horizon when observed from the perspective of freely falling detectors in any of these vacuum states.

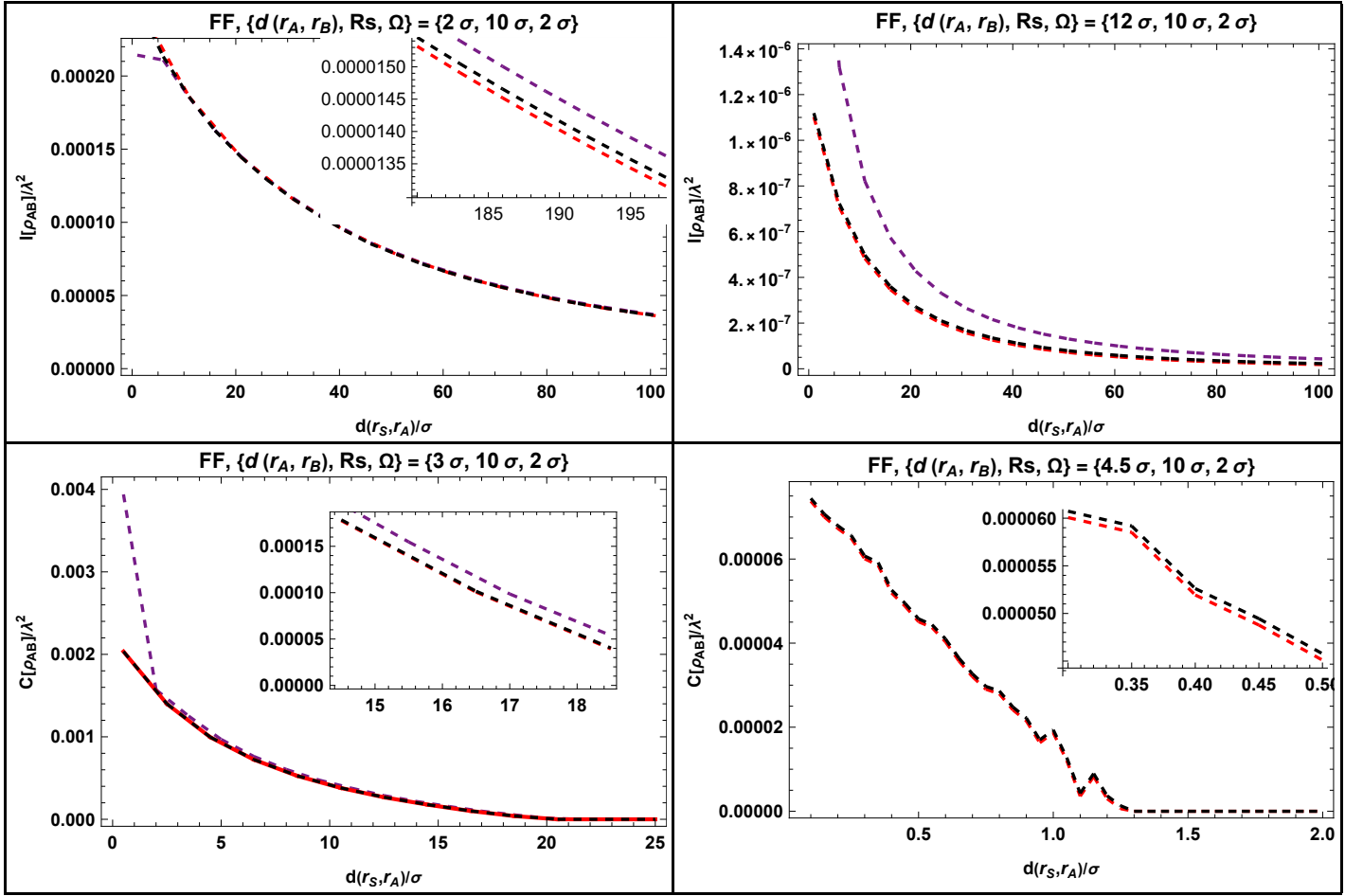


Figure 11: The above figures show the numerical plots of the mutual information (the top panel) and the concurrence (the bottom panel) with two freely falling UDWs as a function of the proper distance of detector A from the event horizon on a constant Painleve-Gullstrand time slice (x-axis) while keeping the distance between two detectors at the peak of Gaussian switching and all other parameters fixed. In the plots, the black line represents the Unruh state, the red line represents the Hartle-Hawking-Israel (HHI) state, and the purple line represents the Boulware state. Here, the two-point function corresponding to the interaction Hamiltonian shown in Eq.(61), $W'_{\psi,c} (= W_{\psi}^{\alpha})$, is taken. We keep $\Omega = 2\sigma$ in all cases.

From Figs. 4, 11, and 12, it is evident that the qualitative behavior of mutual information and concurrence in each of these three vacuum states are quite similar. In particular, we do not observe any decay in correlation measures near the horizon. This observation suggests that the decay near the horizon, observed in subsection 4.2.2, is due to high gravitational acceleration.

In Fig. 12, we have plotted the mutual information and concurrence with two-point functions $W'_{\psi,f}$ defined in (27), $W'_{\psi,f}^{\text{Unruh}}$ defined in (36), and $W'_{\psi,f}^{\text{Boulware}}$ defined in (42). One observes in Fig. 12 that both the mutual information and the concurrence are maximum for the HHI vacuum, while they attain their minimum values for the Boulware vacuum. This ordering can be understood by the enhancement of correlations due to the dominance of the anti-Hawking effect in the HHI state far from the horizon (see Fig 7). This ordering differs to that observed in Fig. 4 and Fig.11 with conformal symmetry obeying two-point functions $W'_{\psi,c}^{\text{HHI}} (= W_{\psi}^{\text{HHI}})$ defined in (20), $W'_{\psi,c}^{\text{Unruh}} (= W_{\psi}^{\text{Unruh}})$ defined in (29) and $W'_{\psi,c}^{\text{Boulware}} (= W_{\psi}^{\text{Boulware}})$ defined in (38). The ordering pattern is the same for both small and large-scale initial separations. Such a behavior can be attributed to the fact that the freely falling detectors need to traverse through the field “bath” (need not be a thermal bath), and in the case of the Unruh vacuum, there is only an outgoing flux of radiation [13; 91]. Meanwhile, in the HHI vacuum, there are both ingoing and outgoing fluxes of radiation (need not be thermal). This difference in radiation fluxes immediately leads to more entanglement disruption in the HHI vacuum. It’s

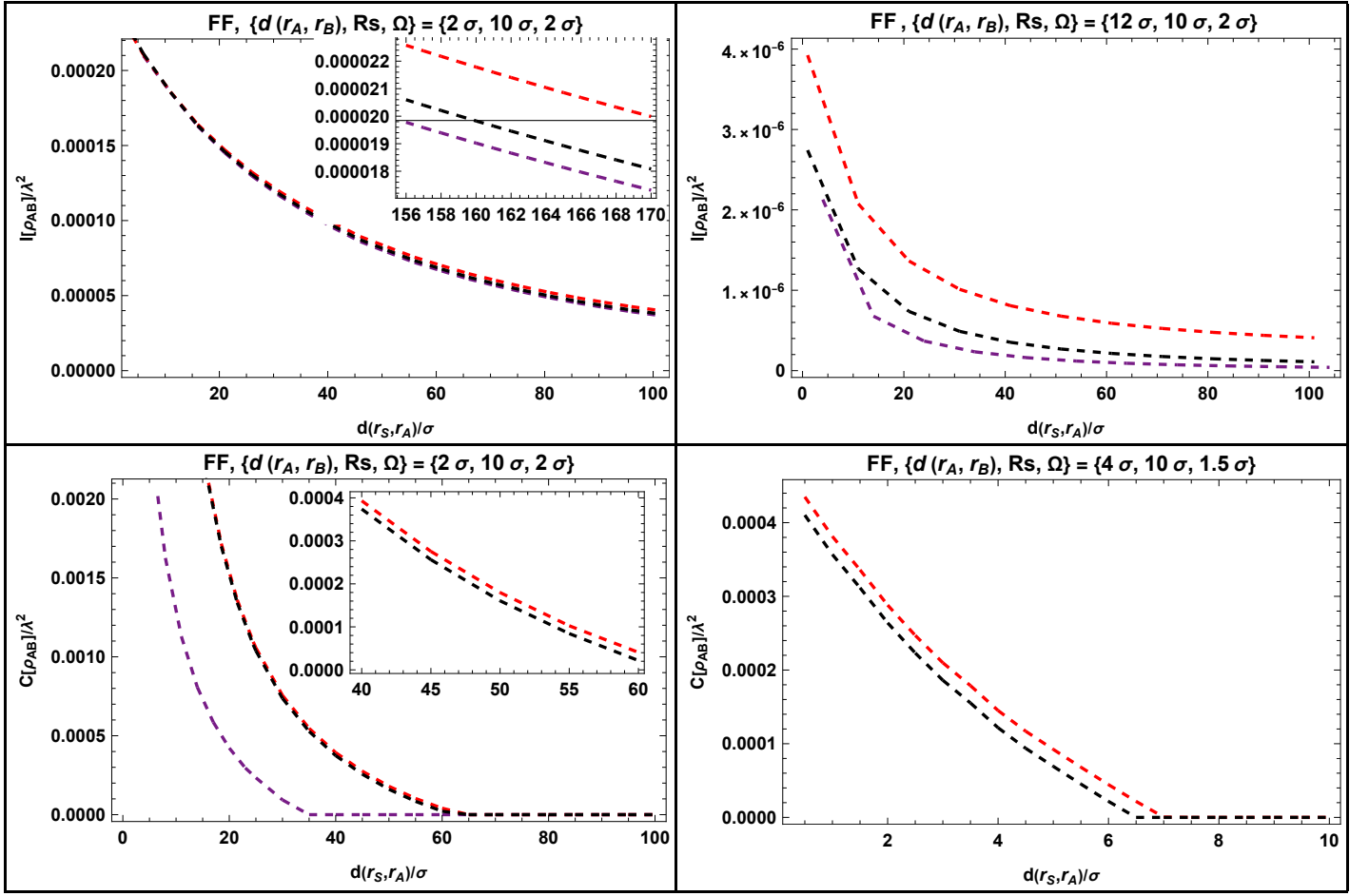


Figure 12: The above figures show the numerical plots of the mutual information (the top panel) and the concurrence (the bottom panel) with two freely falling UDWs as a function of the proper distance of detector A from the event horizon on a constant Painleve-Gullstrand time slice (x-axis) while keeping the distance between two detectors at the peak of Gaussian switching and all other parameters fixed. In the plots, the black line represents the Unruh state, the red line represents the Hartle-Hawking-Israel (HHI) state, and the purple line represents the Boulware state. The interaction Hamiltonian \hat{H}_j^{int} shown in Eq. (62) is used with the freely falling 2-bein, and we keep $\Omega = 2\sigma$ in all cases.

important to highlight that, while keeping the peak of detector A very close to the horizon, the detector does spend some time beyond the horizon due to the long tail of the Gaussian switching function. However, as evident from the plots for both the Unruh and HHI vacua, they exhibit smooth behavior near the horizon. This suggests that the detectors do not experience any sudden or abrupt changes as they cross the black hole horizon. We also note that both the mutual information and the concurrence are finite and smooth as one approaches the event horizon in all cases. We next explore the near-horizon entanglement properties in the next section.

5 Near horizon entanglement of HHI vacuum

The proper distance between two Schwarzschild coordinates at a fixed Schwarzschild time slice and constant θ and ϕ is given by

$$z = \int_{r_A}^{r_B} \frac{1}{\sqrt{1 - \frac{R_s}{r}}} dr. \quad (88)$$

In terms of the proper distance z defined above, the truncated Schwarzschild metric near the event horizon is given by

$$ds^2 \approx -z^2 dt_S^2 + dz^2. \quad (89)$$

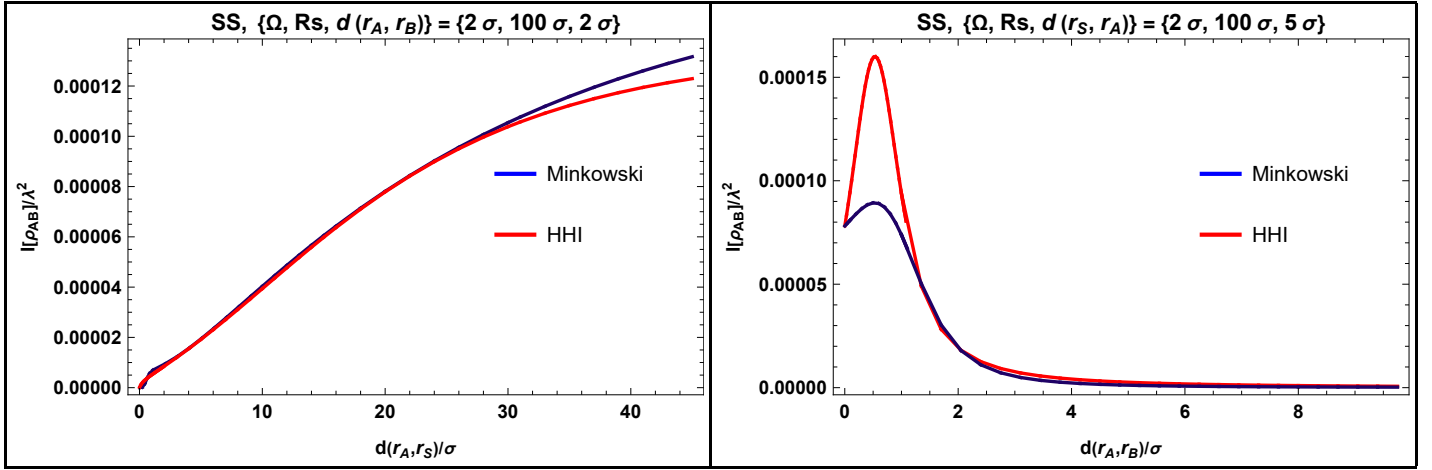


Figure 13: Plots for the comparison of Minkowski and HHI states mutual information near the horizon with two static detectors having coupling \hat{H}_j^{int} shown in Eq.(61).

In terms of $\kappa \equiv (1/2)f'(r = R_s)$ and $l \equiv (r - R_s)$, with $f(r) = (1 - R_s/r)$, the above metric in Eq. (89) is expressed as

$$ds^2 \approx -2\kappa l dt_S^2 + \frac{dl^2}{2\kappa l}. \quad (90)$$

This is precisely the metric of a Rindler observer in flat Minkowski spacetime. The stress-energy tensor for the Unruh vacua exhibits divergences near the past horizons. While the stress-energy tensor for the Boulware vacuum has divergence on both future and past event horizons. The divergence underscores the significance of considering the influence of the matter sector in shaping the spacetime geometry, signaling a deviation from the semiclassical regime in the vicinity of the horizon. In contrast, there is no such divergence for the HHI state. In a flat spacetime scenario, the expectation value of stress energy in the Rindler vacuum is divergent near the horizon, whereas no such divergence is present for the expectation value in the Minkowski vacuum. The equivalence principle implies that the local gravitational effect felt by a static detector is equivalent to an acceleration in Minkowski spacetime. Furthermore, a uniformly accelerating detector in flat space experiences Unruh radiation, analogous to the Hawking radiation encountered by a static detector in the HHI state. These observations prompt us to draw a comparison between the near-horizon properties of the HHI vacuum for a static observer and the Minkowski vacuum for a uniformly accelerated observer, i.e., a Rindler observer.

From Eq.(55), the mutual information between two disjoint intervals in the HHI vacuum is given by

$$I_{\text{HHI}} = \frac{1}{12} \log \left(\frac{(V_1 - V_3)^2 (U_1 - U_3)^2 (V_2 - V_4)^2 (U_2 - U_4)^2}{(V_3 - V_2)^2 (U_3 - U_2)^2 (V_1 - V_4)^2 (U_1 - U_4)^2} \right). \quad (91)$$

In the limit, when the interval A is very close to the future event horizon $U_1 \rightarrow 0$ and $U_2 \rightarrow 0$. Therefore, Eq. (91) becomes

$$I_{\text{HHI}} \approx \frac{1}{12} \log \left(\frac{(V_1 - V_3)^2 (V_2 - V_4)^2}{(V_3 - V_2)^2 (V_1 - V_4)^2} \right). \quad (92)$$

In the same limit $V = 2R_s e^{v/2R_s} \rightarrow 2R_s^{1/2} e^{t_S/2r_s} \sqrt{r - R_s}$. Considering intervals on a $t_S = \text{constant}$ hypersurface, Eq. (92) can be rewritten as

$$I_{\text{HHI}} \approx \frac{1}{12} \log \left(\frac{(\sqrt{r_1 - R_s} - \sqrt{r_3 - R_s})^2 (\sqrt{r_2 - R_s} - \sqrt{r_4 - R_s})^2}{(\sqrt{r_3 - R_s} - \sqrt{r_2 - R_s})^2 (\sqrt{r_1 - R_s} - \sqrt{r_4 - R_s})^2} \right). \quad (93)$$

The mutual information between two disjoint intervals $[(U_{M1}, V_{M1}), (U_{M2}, V_{M2})]$ and $[(U_{M3}, V_{M3}), (U_{M4}, V_{M4})]$ for a Rindler observer in Minkowski vacuum, with (U_{Ms}, V_{Ms}) being the Minkowski null coordinates, is given by

$$I_{\text{Mink}} = \frac{1}{12} \log \left(\frac{(V_{M1} - V_{M3})^2 (U_{M1} - U_{M3})^2 (V_{M2} - V_{M4})^2 (U_{M2} - U_{M4})^2}{(V_{M3} - V_{M2})^2 (U_{M3} - U_{M2})^2 (V_{M1} - V_{M4})^2 (U_{M1} - U_{M4})^2} \right). \quad (94)$$

In the near horizon limit, $U_{M1} \rightarrow 0$, $U_{M2} \rightarrow 0$ and $V_{Ms} \rightarrow \sqrt{2l_s}e^{g\tau}/\sqrt{g}$. Here ‘g’ is the acceleration parameter of the Rindler observer. Furthermore, taking both intervals on $\tau = \text{constant}$ hypersurface Eq.(94) becomes

$$I_{\text{Mink}} \approx \frac{1}{12} \log \left(\frac{(\sqrt{l_1} - \sqrt{l_3})^2 (\sqrt{l_2} - \sqrt{l_4})^2}{(\sqrt{l_3} - \sqrt{l_2})^2 (\sqrt{l_1} - \sqrt{l_4})^2} \right). \quad (95)$$

Identifying $l_s = r - R_s$ we get $I_{\text{Mink}} \approx I_{\text{HHI}}$. Therefore, near the horizon, the mutual information between two nearby disjoint intervals in both situations is equivalent.

To see the equivalence of the entanglement properties from the point of view of an UDW detector, let us consider two UDW detectors, namely A and B, along the following trajectories in the Minkowski vacuum.

$$\left\{ \text{Detector A: } t_A = \frac{1}{g_A} \sinh g_A \tau_A; x_A = \frac{1}{g_A} \cosh g_A \tau_A \right\} \quad (96)$$

$$\left\{ \text{Detector B: } t_B = \frac{1}{g_B} \sinh g_B \tau_B; x_B = \frac{1}{g_B} \cosh g_B \tau_B \right\} \quad (97)$$

where τ_A and τ_B are proper time in the frame of detectors A and B, respectively, x’s and t’s are their Minkowski coordinates, and g_A and g_B are their accelerations. We take events’ common line of simultaneity in both detector frames to pass from the origin of chosen coordinates, namely

$$\frac{t_A}{x_A} = \frac{t_B}{x_B} \quad (98)$$

Imposing the above constraints on trajectories Eqs. (96) and (97) we get

$$\tanh g_A \tau_A = \tanh g_B \tau_B \quad (99)$$

Now, since the arguments are real, we can utilize the fact that hyperbolic functions are one-to-one to write $g_A \tau_A = g_B \tau_B$. Therefore, the trajectory becomes

$$\left\{ \text{Detector A: } t_A = \sqrt{\frac{2l_A}{g}} \sinh g_A \tau_A; x_A = \sqrt{\frac{2l_A}{g}} \cosh g_A \tau_A \right\} \quad (100)$$

$$\left\{ \text{Detector B: } t_B = \sqrt{\frac{2l_B}{g}} \sinh g_A \tau_A; x_B = \sqrt{\frac{2l_B}{g}} \cosh g_A \tau_A \right\} \quad (101)$$

where l_s describe the Rindler coordinates and $g_s = \sqrt{g/2l_s}$. The proper distance between detectors, say, at $t_A = t_B = 0$, is given by

$$-\frac{\sqrt{2gl_A}}{g} + \frac{\sqrt{2gl_B}}{g}.$$

We choose $l_A = 1/2g$ and fix l_B such that the above proper distance corresponds to the same proper distance between detectors in the Schwarzschild metric. Therefore, equating this with Eq. (73) we get,

$$l_B = \frac{1}{2g} \left(1 + g \int_{r_A}^{r_B} \frac{1}{\sqrt{1 - \frac{R_s}{r}}} dr \right)^2 \quad (102)$$

The parameter g is fixed by taking the following local acceleration felt by detector A at r_A in Schwarzschild spacetime:

$$g = \frac{R_s}{2r_A^2 \sqrt{1 - \frac{R_s}{r_A}}}. \quad (103)$$

With the above parameters and the two point function W_ψ^{HHI} shown in Eq.(20), we repeat the entanglement harvesting protocol discussed in section 4.2 for two static UDWs in HHI and two uniformly accelerating UDWs in the Minkowski vacuum. The result is displayed in Fig. 13. One observes from Fig. 13 that the total correlation near the horizon in both of these situations, namely the HHI state for a static observer near the horizon and the Minkowski vacuum for a uniformly accelerated observer follows a similar trend. It is also apparent that as we move farther from the horizon, the disparity in correlations between the two scenarios increases. This observation suggests that the similarity in correlations between the two situations is primarily limited to the vicinity of the horizon.

6 Discussion

We investigated the entanglement features of a massless fermionic field outside a Schwarzschild black hole in various states, namely the Hartle-Hawking-Israel (HHI), Unruh, and Boulware states. The entanglement observed by an observer using a detector depends on several parameters and in order to understand what an observer measures, we employed the entanglement harvesting protocol to study the correlations present in a massless fermionic field, the results of which are summarized below.

As a preliminary to entanglement harvesting, we first analyzed the transition rate of the detector. Specifically, for a static Unruh–DeWitt (UDW) detector coupled to the scalar density of a massless fermionic field—even when it is coupled to the rescaled Hamiltonian \hat{H}_j^{int} shown in Eq. (62)—the transition rate in the HHI state is found to follow a Planckian distribution, as expected. A similar analysis for the UDW detectors coupled with the scalar density of the Fermionic field in the Unruh state yields the Helmholtz free energy of a thermal bath of fermionic fields. However, the same with detectors coupled with rescaled interaction \hat{H}_j^{int} shown in Eq. (62) for the Unruh state yields the Helmholtz free energy of a thermal bath of fermionic or bosonic fields, depending on whether the 2-bein of the chosen interaction Hamiltonian represents 2-velocity of the local Lorentz frame preserving conformal symmetry or is selected based on the requirement that its 2-velocity match the UDW detector’s velocity respectively. The presence of the anti-Hawking effect is found to be dependent on the choice of the interaction Hamiltonian through the 2-bein. If conformal symmetry is broken by the choice of the 2-bein of the interaction Hamiltonian to move with the detector, the anti-Hawking effect arises, reaching its maximum for the HHI state. In particular, for static detectors, the weak anti-Hawking effect intensifies as one approaches the horizon, while for freely falling UDW detectors, the anti-Hawking effect occurs away from the horizon and vanishes near it. In contrast, we found that detectors coupled to the scalar density of the field—whether through the interaction Hamiltonian \hat{H}_j^{int} shown in Eq. (61), or the rescaled interaction Hamiltonian \hat{H}_j^{int} with a conformal-preserving 2-bein—do not experience any anti-Hawking effect.

Using the resolvent technique, we demonstrated that for two sufficiently separated, disjoint regions, the mutual information is minimized in the HHI state and maximized in the Boulware state, provided that the separation between the intervals satisfies specific conditions stated in Appendix [E]. The mutual information between two disjoint regions is known to be invariant under an arbitrary Weyl transformation. If we vary the proper distance between two disjoint intervals, $d(r_A, r_B)$, outside the horizon, then we get a peak in the mutual information calculated using the resolvent technique. The peak corresponds to the position where both regions are almost null-separated. One can control the distance between peak and horizon by varying δ_L , which determines the spatial extent of intervals chosen in the resolvent technique calculation. With these two disjoint intervals, when we compare two UDWs which peak around these intervals approximately and perform entanglement harvesting, we get a single broad peak in the mutual information. This can be interpreted as, although the detector is spatially point-like, it is switched on with a Gaussian switching, and hence the temporal extent in the case of UDW and resolvent technique intervals is not the same. The width of the peaks in all three states is larger when detector A is far from the horizon compared to when it is near the horizon. This can be interpreted as the effects of vacuum polarization and gravitational redshift being large near the horizon, and as a result, the peak dies down quickly. The relative ordering of observed correlations in the UDWs for the three vacua, which matches with those in resolvent technique calculations, suggests that Hawking radiation diminishes entanglement.

Next, we fixed the distance between two detectors and varied the proper distance from the horizon of the detector closest to the horizon at a fixed Painleve-Gullstrand time slice. The relative ordering of correlation measures for different states for the case of rescaled interaction Hamiltonian \hat{H}_j^{int} with a 2-bein moving with the static or freely falling UDW is also found to be the reverse of that of both the conformal symmetry-preserving case with \hat{H}_j^{int} as well as the scalar density Hamiltonian \hat{H}_j^{int} . These observations can be interpreted as the anti-Hawking effect enhances entanglement, since the anti-Hawking effect is absent in the conformal symmetry-preserving case. While the relative ordering of the correlation measures for the case of a 2-bein moving with the static or freely falling UDW suggests that the Hawking radiation diminishes the entanglement. More interestingly, for static detectors with static 2-bein, although some decay of entanglement measures is found near the horizon for all states, we do not get a complete death of entanglement near the horizon. However, the decay is larger, with the conformal symmetry obeying the two-point function $W_{\psi,c}^{\text{State}}$, and the system of UDWs, in this case, harvests no entanglement near the horizon in HHI and Unruh states. We further confirm that the freely falling detectors don’t suffer the phenomenon of entanglement decay near the horizon. In contrast, the harvested entanglement monotonically increases as one moves towards the horizon in the case of freely falling detectors. This behavior is shown to match the resolvent technique calculation. This suggests that another cause of the entanglement decay for the static detectors near the horizon is the local gravitational acceleration felt by the detectors.

We further showed that the near-horizon entanglement features of the HHI vacuum for a static observer, using both the resolvent technique in QFT as well as the UDW detectors numerical calculations, are identical to those for a uniformly

accelerating observer in the Minkowski vacuum in 1+1 dimensions. Entanglement features beyond the event horizon shall remain a topic for future investigation. Here, we restricted our analysis to 1+1 dimensions throughout this manuscript. However, it would be interesting to extend our study to higher dimensions and explore spacetimes beyond Schwarzschild. Notably, the presence of the anti-Hawking effect, which enhances entanglement, depends on the choice of the interaction Hamiltonian. The explicit role of the effective potential, curvature, and kinematics in the anti-Hawking effect remains an open possibility.

Acknowledgements

The authors thank Jorma Louko for his valuable discussions and insightful comments on this manuscript.

Appendices

Appendix A Computing the two point function W_ψ^α

In this appendix, we aim to compute the following normal ordered two-point function for the scalar density of the Fermionic field in the (1+1) dimensional Schwarzschild spacetime:

$$W_\psi^\alpha(x, x') = \langle 0_\alpha | : \bar{\psi}_a(x) \psi_a(x) :: \bar{\psi}_b(x') \psi_b(x') : | 0_\alpha \rangle, \quad (104)$$

where each repeated spinor index is summed over [42; 85]. The index α is used to denote vacua which is being used. It is known that in two dimensions, the conformal anomaly, as well as Hawking flux, are identical for fields with spins of 0 and 1/2, as discussed in reference [50]. Also, there is no gravitational anomaly for the Fermionic field in 1+1 spacetime dimensions[48]. Decomposing the field into positive and negative frequency parts and using normal ordering [42; 85], we get

$$\begin{aligned} W_\psi^\alpha(x, x') &= \langle 0_\alpha | \bar{\psi}_a^+(x) \psi_a^+(x) \bar{\psi}_b^-(x') \psi_b^-(x') | 0_\alpha \rangle \\ &= \langle 0_\alpha | \bar{\psi}_a^+(x) \psi_b^-(x') \psi_a^+(x) \bar{\psi}_b^-(x') | 0_\alpha \rangle \\ &= \langle 0_\alpha | \{ \bar{\psi}_a^+(x), \psi_b^-(x') \} \{ \psi_a^+(x), \bar{\psi}_b^-(x') \} | 0_\alpha \rangle \\ &= i S_{ba}^-(x', x) i S_{ab}^+(x, x') \\ &= -Tr[S^+(x, x') S^-(x', x)] \\ &= -Tr[\tilde{\gamma}^\mu(x) U(x, x') \tilde{\gamma}^\nu(x') U(x', x) \nabla_\mu^x W_\phi^\alpha(x, x') \nabla_\nu^{x'} W_\phi^\alpha(x, x')] \end{aligned} \quad (105)$$

Here, we have used $\langle 0_\alpha | \psi_b^- = 0, \psi_a^+ | 0_\alpha \rangle = 0$ in the third line and Eq.(11) with $m=0$ in the in the 6th line. Furthermore, we assume throughout that $\tilde{\gamma}^\mu \nabla_\mu U(x, x') = 0$ for the parallel transport along the geodesic. Using $U(x, x') \tilde{\gamma}^\nu(x') U(x', x) = \tilde{\gamma}^\rho(x) \Lambda_\rho^\nu(x', x)$, where $\Lambda_\rho^\nu(x', x)$ represents the vector parallel propagator [51; 52; 53; 54] one gets

$$\begin{aligned} W_\psi^\alpha(x, x') &= -Tr[\tilde{\gamma}^\mu(x) \tilde{\gamma}^\rho(x) \Lambda_\rho^\nu(x', x) \nabla_\mu^x W_\phi^\alpha(x, x') \nabla_\nu^{x'} W_\phi^\alpha(x, x')] \\ &= -Tr[b_\delta^\mu(x) \gamma^\delta b_\beta^\rho(x) \gamma^\beta \Lambda_\rho^\nu(x', x) \nabla_\mu^x W_\phi^\alpha(x, x') \nabla_\nu^{x'} W_\phi^\alpha(x, x')] \\ &= -Tr[b_\delta^\mu(x) b_\beta^\rho(x) \eta^{\delta\beta} \mathbb{1} \Lambda_\rho^\nu(x', x) \nabla_\mu^x W_\phi^\alpha(x, x') \nabla_\nu^{x'} W_\phi^\alpha(x, x')] \end{aligned}$$

Here, $b(\dots)$ denotes the 2-bein, which has been used to express the curved spacetime Dirac gamma matrices $\tilde{\gamma}^\mu$ in terms of the flat spacetime gamma matrices γ^δ in the second line. In the third line, we have used the anticommutator relation of Dirac matrices $\{\gamma^\delta, \gamma^\beta\} = 2\mathbb{1} \eta^{\delta\beta}$. Since all indices are contracted, we can write everything else other than $\mathbb{1}$ as C to give the following:

$$\begin{aligned} W_\psi^\alpha(x, x') &= -Tr[C \mathbb{1}] \\ &= -N b_\delta^\mu(x) b_\beta^\rho(x) \eta^{\delta\beta} \Lambda_\rho^\nu(x', x) \partial_\mu^x W_\phi^\alpha(x, x') \partial_\nu^{x'} W_\phi^\alpha(x, x'). \end{aligned} \quad (106)$$

$$= -N g^{\mu\rho}(x) \Lambda_\rho^\nu(x', x) \partial_\mu^x W_\phi^\alpha(x, x') \partial_\nu^{x'} W_\phi^\alpha(x, x') \quad (107)$$

Since W_ϕ^α represents the Wightman function of a scalar field in the corresponding vacuum, we can write the spinor covariant derivative as a partial derivative, and use the identity $\text{Tr}[C\mathbf{1}] = NC$, where N is the dimensionality of the spacetime, to evaluate the trace and get the second line. In the final expression, (107), we use $b_\delta^\mu(x)b_\beta^\rho(x)\eta^{\delta\beta} = g^{\mu\rho}(x)$.

The Wightman function of a real massless scalar field in different states are given by [50]

$$W_\phi^{\text{Boulware}} = -\frac{1}{4\pi} \ln[-\zeta^2(\Delta u - i\epsilon)(\Delta v - i\epsilon)] \quad (108)$$

$$W_\phi^{\text{Unruh}} = -\frac{1}{4\pi} \ln[-\zeta^2(\Delta U - i\epsilon)(\Delta v - i\epsilon)] \quad (109)$$

$$W_\phi^{\text{HHI}} = -\frac{1}{4\pi} \ln[-\zeta^2(\Delta U - i\epsilon)(\Delta V - i\epsilon)] \quad (110)$$

where, $\zeta > 0$ is an IR cutoff. Since the two-point function for the scalar density of the massless spin-1/2 field is infrared-safe, we can ignore the parameter Λ for further calculations. By repeating the above calculation for the two point function shown in Eq.(17) one gets

$$\begin{aligned} W_{\psi,b}^{\prime\alpha}(x,x') &= \langle 0_\alpha | \bar{\psi}'^+_a(x) \psi'^+_a(x) \bar{\psi}'^-_b(x') \psi'^-_b(x') | 0_\alpha \rangle \\ &= \langle 0_\alpha | \bar{\psi}'^+_a(x) \psi'^-_b(x') \psi'^+_a(x) \bar{\psi}'^-_b(x') | 0_\alpha \rangle \\ &= \langle 0_\alpha | \{ \bar{\psi}'^+_a(x), \psi'^-_b(x') \} \{ \psi'^+_a(x), \bar{\psi}'^-_b(x') \} | 0_\alpha \rangle \\ &= -\text{Tr}[\bar{A}(x)A(x')S^+(x,x')A(x)\bar{A}(x')S^-(x',x)] \\ &= -\text{Tr}[\bar{A}(x)A(x')\tilde{\gamma}^\mu(x)U(x,x')A(x)\bar{A}(x')\tilde{\gamma}^\nu(x')U(x',x)\nabla_\mu^x W_\phi^\alpha(x,x')\nabla_\nu^{x'} W_\phi^\alpha(x,x')] \\ &= -\text{Tr}[U(x,x')\tilde{\gamma}^\mu(x)\tilde{\gamma}^\nu(x')U(x',x)\nabla_\mu^x W_\phi^\alpha(x,x')\nabla_\nu^{x'} W_\phi^\alpha(x,x')] \\ &= -\text{Tr}[U(x,x')b_\delta^\mu(x)\gamma^\delta b_\beta^\nu(x')\gamma^\beta U(x',x)\nabla_\mu^x W_\phi^\alpha(x,x')\nabla_\nu^{x'} W_\phi^\alpha(x,x')] \end{aligned} \quad (111)$$

Here, we have used the relations $A(x)\bar{A}(x') = U(x',x)$ and $U(x',x)U(x,x') = \mathbf{1}$ in the second last (sixth) line. Comparing the second last equation in Eq.(111) with the last equation in Eq.(105), one can check that the ordering of the $U(x,x')$ s and the $\tilde{\gamma}^\mu(x)$ are different which leads to the 2-bein dependence in the final expression. Using $\text{Tr}[XY] = \text{Tr}[YX]$ and then again $U(x',x)U(x,x') = \mathbf{1}$ one can get rid of the spin parallel propagator as follows.

$$\begin{aligned} W_{\psi,b}^{\prime\alpha}(x,x') &= -\text{Tr}[b_\beta^\nu(x')\gamma^\beta U(x',x)U(x,x')b_\delta^\mu(x)\gamma^\delta \nabla_\mu^x W_\phi^\alpha(x,x')\nabla_\nu^{x'} W_\phi^\alpha(x,x')] \\ &= -\text{Tr}[b_\beta^\nu(x')\gamma^\beta b_\delta^\mu(x)\gamma^\delta \nabla_\mu^x W_\phi^\alpha(x,x')\nabla_\nu^{x'} W_\phi^\alpha(x,x')] \\ &= -\text{Tr}[b_\beta^\nu(x')b_\delta^\mu(x)\eta^{\delta\beta} \mathbf{1} \partial_\mu^x W_\phi^\alpha(x,x')\partial_\nu^{x'} W_\phi^\alpha(x,x')] \\ &= -\text{Tr}[C'\mathbf{1}] \\ &= -Nb_\beta^\nu(x')b_\delta^\mu(x)\eta^{\delta\beta} \partial_\mu^x W_\phi^\alpha(x,x')\partial_\nu^{x'} W_\phi^\alpha(x,x'). \end{aligned} \quad (112)$$

In the third line, we have used the anticommutator relation of the Dirac matrices, $\{\gamma^\delta, \gamma^\beta\} = 2\mathbf{1}\eta^{\delta\beta}$. Since all indices are contracted, we can again express everything other than $\mathbf{1}$ as C' and again use the identity $\text{Tr}[C'\mathbf{1}] = NC'$, where N is the dimensionality of spacetime, to obtain the final expression, Eq. (112). One can notice that the Eq. (112) is now dependent on the 2-beins at x and x' , because of the presence of A and \bar{A} in the transformed field ψ' which cancels with the spin parallel propagator term.

Appendix B Response rate of a static detector in the HHI state

The pullback of the two-point function shown in Eq. (25) along the trajectory of a static detector is given by,

$$\begin{aligned} W_{\psi,s}^{\text{HHI}}(x(\tau), x(\tau')) &= -\frac{1}{4\pi^2 \sqrt{1-R_s/r} \sqrt{1-R_s/r'}} \left[e^{(v'-u)/2R_s} + e^{(v-u')/2R_s} \right] \frac{1}{(\Delta U - i\epsilon)(\Delta V - i\epsilon)} \\ &= -\frac{1}{32\pi^2 R_s^2 (1 - \frac{R_s}{r})} \frac{\cosh(t'_S - t_S)/2R_s}{\sinh^2\left(\frac{t'_S - t_S - i\epsilon}{4R_s}\right)}. \end{aligned}$$

Here, we have used $U = -2R_s e^{-u/2R_s}$ and $V = 2R_s e^{v/2R_s}$, where $u = t_S - r_*$ and $v = t_S + r_*$ with $r = r'$ in the second line. For a static detector, $d\tau = \sqrt{1 - R_s/r} dt_S = \kappa dt_S$ (say). Therefore, the above expression becomes

$$W'_{\psi,s}{}^{\text{HHI}}(x(\tau), x(\tau')) = -\frac{1}{32\pi^2 R_s^2 \kappa^2} \frac{\cosh \Delta\tau/2\kappa R_s}{\sinh^2 \left(\frac{\Delta\tau - i\epsilon}{4R_s \kappa} \right)} \quad (113)$$

Using the periodicity in the imaginary time of the above expression one can see the KMS thermality of the HHI state. Substituting for $W'_{\psi,s}{}^{\text{HHI}}$ from Eq.(113) in Eq.(69), we get the following transition rate

$$\begin{aligned} \dot{\mathcal{F}} &= -\frac{1}{32\pi^2 R_s^2 \kappa^2} \int_{-\infty}^{\infty} d\Delta\tau e^{-i\Omega\Delta\tau} \frac{\cosh \Delta\tau/2\kappa R_s}{\sinh^2 \left(\frac{\Delta\tau - i\epsilon}{4R_s \kappa} \right)} \\ &= -\frac{1}{32\pi^4 R_s^2 \kappa^2} \sum_{k=-\infty}^{k=\infty} \int_{-\infty}^{\infty} d\Delta\tau \frac{e^{-i\Omega\Delta\tau} \cosh \Delta\tau/2\kappa R_s}{\left(\frac{\Delta\tau - i\epsilon}{4\pi R_s \kappa i} - k \right)^2} \\ &= \frac{1}{2\pi^2} \sum_{k=-\infty}^{k=\infty} \int_{-\infty}^{\infty} d\Delta\tau \frac{e^{-i\Omega\Delta\tau} \cosh \Delta\tau/2\kappa R_s}{\left(\Delta\tau - i\epsilon - i4\pi k R_s \kappa \right)^2}, \end{aligned}$$

where we have used $\text{cosec}^2 \pi x = \pi^{-2} \sum_{k=-\infty}^{k=\infty} (x - k)^{-2}$ in the second line. By choosing contour in the lower half plane to do this integration, we get

$$\dot{\mathcal{F}} = \frac{\Omega}{\pi} \sum_{k=1}^{k=\infty} e^{-4\pi k R_s \Omega} = \frac{\Omega}{\pi(e^{4\pi R_s \Omega} - 1)}. \quad (114)$$

Appendix C Response rate of a static detector in the Unruh state

The pullback of two-point function in Eq.(34) along the trajectory of a static detector is given by,

$$\begin{aligned} W'_{\psi,s}{}^{\text{Unruh}}(x, x') &= -\frac{1}{4\pi^2 \sqrt{1 - R_s/r} \sqrt{1 - R_s/r'}} \left[e^{-u/2R_s} + e^{-u'/2R_s} \right] \frac{1}{(\Delta U - i\epsilon)(\Delta v - i\epsilon)} \\ &= -\frac{1}{8\pi^2 R_s (1 - \frac{R_s}{r})} \frac{\cosh \left(\frac{t'_S - t_S}{4R_s} \right)}{\sinh \left(\frac{t'_S - t_S - i\epsilon}{4R_s} \right) (t'_S - t_S - i\epsilon)}. \end{aligned} \quad (115)$$

Substituting the above expression in Eq.(69), we get the following transition rate:

$$\begin{aligned} \dot{\mathcal{F}} &= -\frac{1}{8\pi^2 R_s \kappa} \int_{-\infty}^{\infty} d\Delta\tau e^{-i\Omega\Delta\tau} \frac{\cosh \left(\frac{\Delta\tau}{4R_s \kappa} \right)}{\sinh \left(\frac{\Delta\tau - i\epsilon}{4R_s \kappa} \right) (\Delta\tau - i\epsilon)} \\ &= \frac{1}{4\pi^2 R_s \kappa} \sum_{n=1}^{\infty} \frac{e^{-4\pi n R_s \Omega}}{n}. \end{aligned} \quad (116)$$

Here, we have used the contour in the lower half plane and summed all residues to write the second line. Summing the infinite series one obtains

$$\dot{\mathcal{F}} = \frac{1}{4\pi^2 R_s \kappa} \log \frac{e^{4\pi\kappa R_s \Omega}}{(e^{4\pi\kappa R_s \Omega} - 1)}. \quad (117)$$

Using expansion of $\log(x+1)$ about $x=1$ we get the following series for the transition rate,

$$\dot{\mathcal{F}}(\Omega) = \frac{1}{4\pi^2 R_s \kappa} \left[\frac{1}{e^{4\pi\kappa R_s \Omega} - 1} - \frac{1}{2} \left(\frac{1}{e^{4\pi\kappa R_s \Omega} - 1} \right)^2 + \frac{1}{3} \left(\frac{1}{e^{4\pi\kappa R_s \Omega} - 1} \right)^3 + \dots \right]. \quad (118)$$

Repeating the above calculation with the 2-bein (30) one gets similar expression in Eq.(116), without cosh factor in the nominator. Therefore, we get the transition rate

$$\dot{\mathcal{F}} = \frac{1}{4\pi^2 R_s \kappa} \sum_{k=1}^{\infty} \frac{(-1)^{k+1} e^{-4\pi\kappa R_s \Omega k}}{k}. \quad (119)$$

Performing the series sum in the above expression, we get

$$\dot{\mathcal{F}}(\Omega) = \frac{1}{4\pi^2 R_s \kappa} \log \frac{e^{4\pi\kappa R_s \Omega}}{(e^{4\pi\kappa R_s \Omega} + 1)}. \quad (120)$$

Appendix D Computing transition probability

In this appendix, we apply the saddle point approximation to compute the diagonal terms of ρ_{AB} , known as the transition probability [94; 107]. The transition probability is given by the following type of integration

$$\begin{aligned} L &= \lambda^2 \int_{-\infty}^{+\infty} d\tau \int_{-\infty}^{+\infty} d\tau' \chi(\tau) \chi(\tau') e^{-i\Omega(\tau-\tau')} W_{\psi}^{\alpha}(x(\tau), x(\tau')) \\ &= \lambda^2 \int_{-\infty}^{+\infty} d\tau \int_{-\infty}^{+\infty} d\tau' e^{-\frac{(\tau-\tau_0)^2}{2\sigma^2}} e^{-\frac{(\tau'-\tau_0)^2}{2\sigma^2}} e^{-i\Omega(\tau-\tau')} W_{\psi}^{\alpha}(x(\tau), x(\tau')) \\ &= \lambda^2 e^{-\sigma^2 \Omega^2} \int_{-\infty}^{+\infty} d\tau \int_{-\infty}^{+\infty} d\tau' e^{-\frac{(\tau-\tau_0+i\Omega\sigma^2/2)^2}{2\sigma^2}} e^{-\frac{(\tau'-\tau_0-i\Omega\sigma^2/2)^2}{2\sigma^2}} W_{\psi}^{\alpha}(x(\tau), x(\tau')). \end{aligned}$$

Now we use the fact that in the case of static detector $W_{\psi}^{\alpha}(x(\tau), x(\tau'))$ is a function of $\tau - \tau'$ viz, it depends only on the interval of time. Changing variables from τ, τ' to $\tilde{x} = \tau + \tau'$ and $\tilde{y} = \tau - \tau'$ one gets

$$L = \lambda^2 e^{-\sigma^2 \Omega^2} \int_{-\infty}^{+\infty} d\tilde{x} \int_{-\infty}^{+\infty} d\tilde{y} e^{-\frac{(\tilde{y}+i2\Omega\sigma^2)^2}{4\sigma^2}} e^{-\frac{(\tilde{x}-2\tau_0)^2}{4\sigma^2}} W_{\psi}^{\alpha}(x(\frac{\tilde{x}+\tilde{y}}{2}), x(\frac{\tilde{x}-\tilde{y}}{2})).$$

Shifting the contour in an imaginary direction for \tilde{y} by $2\Omega\sigma^2$ makes the exponential factors real. Now, the saddle point approximation on the resulting expression gives [94; 107]

$$L \approx 2\pi\sigma^2 \lambda^2 e^{-\sigma^2 \Omega^2} W_{\psi}^{\alpha}(x(\tau_0 - i\Omega\sigma^2), x(\tau_0 + i\Omega\sigma^2)) + \text{residue terms}. \quad (121)$$

The residue term that comes from shifting the contour vanishes if one restricts to $\Omega\sigma^2/2\kappa R_s < \pi$, as no pole is being crossed.

Appendix E Monotonicity of $h(x)$ and $g(x)$

Let us define a function $h(x)$ as

$$h(x) = \frac{x_2 - x}{e^{-x_2} - e^{-x}} \frac{e^{-x_1} - e^{-x}}{x_1 - x}. \quad (122)$$

The sign of the denominator of the first derivative of the above function is positive since we get a square after differentiation. Therefore, the overall sign is determined by the numerator, which is given by

$$\begin{aligned}\text{sign}(h'(x)) &= \text{sign}[(x_2 - x_1)(e^{-x_1-x_2} + e^{-2x}) + (x_1x_2 - (x_1 + x_2)x + x^2 + x_1 - x_2)e^{-x-x_2} \\ &\quad - (x_1x_2 - (x_1 + x_2)x + x^2 + x_2 - x_1)e^{-x-x_1}] \\ &= \text{sign}[(x_2 - x_1)(e^{x-x_1} + e^{-x+x_2}) + (x_1x_2 - (x_1 + x_2)x + x^2 + x_1 - x_2) \\ &\quad - (x_1x_2 - (x_1 + x_2)x + x^2 + x_2 - x_1)e^{x_2-x_1}].\end{aligned}\quad (123)$$

Assuming the points x_1 and x_2 are close together, we can ignore quadratic and higher-order terms in the expansion of $e^{x_2-x_1}$. Keeping terms linear in $x_2 - x_1$, we obtain:

$$\text{sign}(h'(x)) = \text{sign}[(x_2 - x_1)(e^{x-x_1} + e^{-x+x_2} - x^2 + (x_2 + x_1)x - x_1x_2 - x_2 + x_1 - 2)].$$

If $x_1 > x_2 > x$ and if x_1 and x_2 are sufficiently larger than x , then e^{-x+x_2} will be dominant and we will have

$$\text{sign}(e^{x-x_1} + e^{-x+x_2} - x^2 + (x_2 + x_1)x - x_1x_2 - x_2 + x_1 - 2) > 0. \quad (124)$$

This implies $h'(x) < 0$. In other words, under these assumptions, $h(x)$ is a monotonically decreasing function of x . Furthermore, one can see that if $x_1 < x_2 < x$, and x_3 and x_4 are sufficiently larger than x_2 , then the e^{x-x_2} term will be dominant. The terms in the second bracket, Eq. (124), as well as the first term, will be positive, which implies that $h'(x) > 0$. In this case $h(x)$ will be a monotonically increasing function of x .

Further, let us define another function $g(x)$ as

$$g(x) = \frac{x_2 - x}{e^{x_2} - e^x} \frac{e^{x_1} - e^x}{x_1 - x}. \quad (125)$$

The sign of the denominator of the first derivative of the above function is also positive since we get a square after differentiation. Therefore, the overall sign is determined by the nominator, which is given by

$$\begin{aligned}\text{sign}(g'(x)) &= \text{sign}[(x_2 - x_1)(e^{x_1+x_2} + e^{2x}) + (-x_1x_2 + (x_1 + x_2)x - x^2 + x_1 - x_2)e^{x+x_2} \\ &\quad + (x_1x_2 - (x_1 + x_2)x + x^2 - x_2 + x_1)e^{x+x_1}] \\ &= \text{sign}[(x_2 - x_1)(e^{x_1-x} + e^{x-x_2}) + (-x_1x_2 + (x_1 + x_2)x - x^2 + x_1 - x_2) \\ &\quad + (x_1x_2 - (x_1 + x_2)x + x^2 + x_1 - x_2)e^{x_1-x_2}]\end{aligned}\quad (126)$$

Once again, assuming the points x_1 and x_2 to be close together, we can ignore quadratic and higher-order terms in the expansion of $e^{x_2-x_1}$. Keeping terms linear in $x_2 - x_1$, we obtain:

$$\text{sign}(g'(x)) = \text{sign}[(x_2 - x_1)(e^{x-x_2} + e^{-x+x_1} - x^2 + (x_2 + x_1)x - x_1x_2 - x_1 + x_2 - 2)].$$

If $x_1 < x_2 < x$ and if x is sufficiently larger than x_1 and x_2 , then e^{x-x_2} will be dominant and we will have

$$\text{sign}(e^{x-x_2} + e^{-x+x_1} - x^2 + (x_2 + x_1)x - x_1x_2 - x_1 + x_2 - 2) > 0. \quad (127)$$

This implies $g'(x) > 0$. In other words, under these assumptions, $g(x)$ is a monotonically increasing function of x . Furthermore, one can see that if $x_1 > x_2 > x$, and x_1 and x_2 are sufficiently larger than x , then the e^{-x+x_1} term will be dominant. The terms in the second bracket, Eq.(127), will be positive while the term in the second bracket will be negative, which implies that $g'(x) < 0$. In this case, $g(x)$ will be a monotonically decreasing function of x .

References

- [1] D. Doren and Harasymiw. Resolving the information paradox with probabilistic spacetime. *Journal of High Energy Physics, Gravitation and Cosmology*, 2023.
- [2] M. El Naschie. A resolution of the black hole information paradox via transfinite set theory. *World Journal of Condensed Matter Physics*, 5, 249-260., 2015.
- [3] David A. Lowe and Larus Thorlacius. AdS / CFT and the information paradox. *Phys. Rev. D*, 60:104012, 1999.

- [4] Suvrat Raju. Lessons from the information paradox. *Phys. Rept.*, 943:1–80, 2022.
- [5] Paolo Zanardi, Daniel A. Lidar, and Seth Lloyd. Quantum tensor product structures are observable induced. *Phys. Rev. Lett.*, 92:060402, Feb 2004.
- [6] João G. A. Caribé, Robert H. Jonsson, Marc Casals, Achim Kempf, and Eduardo Martín-Martínez. Lensing of vacuum entanglement near schwarzschild black holes. *Phys. Rev. D*, 108:025016, Jul 2023.
- [7] Mehdi Saravani, Siavash Aslanbeigi, and Achim Kempf. Spacetime curvature in terms of scalar field propagators. *Phys. Rev. D*, 93:045026, Feb 2016.
- [8] Achim Kempf. Replacing the Notion of Spacetime Distance by the Notion of Correlation. *Front. in Phys.*, 9:247, 2021.
- [9] Thomas Faulkner, Thomas Hartman, Matthew Headrick, Mukund Rangamani, and Brian Swingle. Snowmass white paper: Quantum information in quantum field theory and quantum gravity. In *Snowmass 2021*, 3 2022.
- [10] Zeng-Bing Chen. The Information-Complete Quantum Theory. *Quantum Eng.*, 2022:9203196, 2022.
- [11] Erickson Tjoa and Robert B. Mann. Harvesting correlations in Schwarzschild and collapsing shell spacetimes. *JHEP*, 08:155, 2020.
- [12] Ireneo James Membrere, Kensuke Gallock-Yoshimura, Laura J. Henderson, and Robert B. Mann. Tripartite Entanglement Extraction from the Black Hole Vacuum. 4 2023.
- [13] Kensuke Gallock-Yoshimura, Erickson Tjoa, and Robert B. Mann. Harvesting entanglement with detectors freely falling into a black hole. *Phys. Rev. D*, 104:025001, Jul 2021.
- [14] Nitesh K. Dubey and Sanved Kolekar. Wigner distributions in rindler spacetime and nonvacuum minkowski states. *Phys. Rev. D*, 111:065004, Mar 2025.
- [15] Baocheng Zhang, Qing-yu Cai, Li You, and Ming-sheng Zhan. Hidden Messenger Revealed in Hawking Radiation: A Resolution to the Paradox of Black Hole Information Loss. *Phys. Lett. B*, 675:98–101, 2009.
- [16] Steven B. Giddings and Yinbo Shi. Quantum information transfer and models for black hole mechanics. *Phys. Rev. D*, 87:064031, Mar 2013.
- [17] Carlos Barcelo, Stefano Liberati, and Matt Visser. Analogue gravity. *Living Rev. Rel.*, 8:12, 2005.
- [18] Antony Valentini. Non-local correlations in quantum electrodynamics. *Physics Letters A*, 153(6-7):321–325, March 1991.
- [19] Benni Reznik. Entanglement from the vacuum. *Found. Phys.*, 33:167–176, 2003.
- [20] Asher Peres, Petra F. Scudo, and Daniel R. Terno. Quantum entropy and special relativity. *Phys. Rev. Lett.*, 88:230402, May 2002.
- [21] Asher Peres and Daniel R. Terno. Quantum information and relativity theory. *Rev. Mod. Phys.*, 76:93–123, 2004.
- [22] Paul M. Alsing and G. J. Milburn. Teleportation with a uniformly accelerated partner. *Phys. Rev. Lett.*, 91:180404, Oct 2003.
- [23] T. Rick Perche and Ahmed Shalabi. Spacetime curvature from ultrarapid measurements of quantum fields. *Phys. Rev. D*, 105:125011, Jun 2022.
- [24] Eduardo Martín-Martínez, T. Rick Perche, and Bruno de S. L. Torres. General relativistic quantum optics: Finite-size particle detector models in curved spacetimes. *Phys. Rev. D*, 101:045017, Feb 2020.
- [25] Eduardo Martín-Martínez, T. Rick Perche, and Bruno de S. L. Torres. Broken covariance of particle detector models in relativistic quantum information. *Phys. Rev. D*, 103:025007, Jan 2021.

- [26] T. Rick Perche, José Polo-Gómez, Bruno de S. L. Torres, and Eduardo Martín-Martínez. Fully relativistic entanglement harvesting. *Phys. Rev. D*, 109:045018, Feb 2024.
- [27] Bruno de Souza Leão Torres. *Aspects of Quantum Information in Quantum Field Theory: Particle detector models, entanglement, and complexity*. PhD thesis, Waterloo U., 2024.
- [28] Maximilian H. Rued. Weakly coupled local particle detectors cannot harvest entanglement. *Class. Quant. Grav.*, 38(19):195029, 2021.
- [29] T. Rick Perche, Caroline Lima, and Eduardo Martín-Martínez. Harvesting entanglement from complex scalar and fermionic fields with linearly coupled particle detectors. *Phys. Rev. D*, 105:065016, Mar 2022.
- [30] Subhajit Barman, Dipankar Barman, and Bibhas Ranjan Majhi. Entanglement harvesting from conformal vacuums between two Unruh-DeWitt detectors moving along null paths. *JHEP*, 09:106, 2022.
- [31] Pratyusha Chowdhury and Bibhas Ranjan Majhi. Fate of entanglement between two Unruh-DeWitt detectors due to their motion and background temperature. *JHEP*, 05:025, 2022.
- [32] Yasusada Nambu. Entanglement structure in expanding universes. *Entropy*, 15(5):1847–1874, 2013.
- [33] Alejandro Pozas-Kerstjens and Eduardo Martín-Martínez. Harvesting correlations from the quantum vacuum. *Phys. Rev. D*, 92:064042, Sep 2015.
- [34] Héctor Maeso-García, José Polo-Gómez, and Eduardo Martín-Martínez. How measuring a quantum field affects entanglement harvesting. *Phys. Rev. D*, 107:045011, Feb 2023.
- [35] Laura J. Henderson, Robie A. Hennigar, Robert B. Mann, Alexander R. H. Smith, and Jialin Zhang. Harvesting Entanglement from the Black Hole Vacuum. *Class. Quant. Grav.*, 35(21):21LT02, 2018.
- [36] Miguel Montero, Juan Leon, and Eduardo Martin-Martinez. Fermionic entanglement extinction in non-inertial frames. *Phys. Rev. A*, 84:042320, 2011.
- [37] Eduardo Martin-Martinez and Juan Leon. Are Alice and Rob really protected by statistics as she falls into a black hole? *Phys. Rev. A*, 80:042318, 2009.
- [38] Nicolai Friis, David Edward Bruschi, Jorma Louko, and Ivette Fuentes. Motion generates entanglement. *Phys. Rev. D*, 85:081701, 2012.
- [39] Eduardo Martín-Martínez and Juan León. Quantum correlations through event horizons: Fermionic versus bosonic entanglement. *Phys. Rev. A*, 81:032320, Mar 2010.
- [40] Ivette Fuentes, Robert B. Mann, Eduardo Martín-Martínez, and Shahpoor Moradi. Entanglement of dirac fields in an expanding spacetime. *Phys. Rev. D*, 82:045030, Aug 2010.
- [41] Shin Takagi. Vacuum Noise and Stress Induced by Uniform Acceleration: Hawking-Unruh Effect in Rindler Manifold of Arbitrary Dimension. *Progress of Theoretical Physics Supplement*, 88:1–142, 03 1986.
- [42] Jorma Louko and Vladimir Toussaint. Unruh-DeWitt detector’s response to fermions in flat spacetimes. *Phys. Rev. D*, 94(6):064027, 2016.
- [43] Wan Mohamad Husni Wan Mokhtar. Radiation from a receding mirror: Unruh-DeWitt detector distinguishes a Dirac fermion from a scalar boson. *Class. Quant. Grav.*, 37(7):075011, 2020.
- [44] Laura J. Henderson, Robie A. Hennigar, Robert B. Mann, Alexander R.H. Smith, and Jialin Zhang. Anti-hawking phenomena. *Physics Letters B*, 809:135732, 2020.
- [45] S. W. Hawking and G. F. R. Ellis. *The Large Scale Structure of Space-Time*. Cambridge Monographs on Mathematical Physics. Cambridge University Press, 1973.
- [46] P. G. Bergmann, M. Cahen, and A. B. Komar. Spherically Symmetric Gravitational Fields. *Journal of Mathematical Physics*, 6(1):1–5, January 1965.

- [47] Robert M. Wald. *General Relativity*. Chicago Univ. Pr., Chicago, USA, 1984.
- [48] Leonard Parker and David Toms. *Quantum Field Theory in Curved Spacetime: Quantized Fields and Gravity*. Cambridge Monographs on Mathematical Physics. Cambridge University Press, 2009.
- [49] David G. Boulware. Spin- $\frac{1}{2}$ quantum field theory in schwarzschild space. *Phys. Rev. D*, 12:350–367, Jul 1975.
- [50] N. D. Birrell and P. C. W. Davies. *Quantum Fields in Curved Space*. Cambridge Monographs on Mathematical Physics. Cambridge University Press, 1982.
- [51] Wolfgang Mück. Spinor parallel propagator and green function in maximally symmetric spaces. *Journal of Physics A: Mathematical and General*, 33(15):3021–3026, 2000.
- [52] B. Allen and C. A. Lütken. Spinor two-point functions in maximally symmetric spaces. *Communications in Mathematical Physics*, 106:201–210, 1986.
- [53] Vasileios A. Letsios. The eigenmodes for spinor quantum field theory in global de Sitter space-time. *J. Math. Phys.*, 62(3):032303, 2021.
- [54] Ivan G. Avramidi. *Heat Kernel and Quantum Gravity*, volume 64 of *Lecture Notes in Physics Monographs*. Springer Berlin, Heidelberg, 2000.
- [55] H. Casini and M. Huerta. Entanglement entropy in free quantum field theory. *J. Phys. A*, 42:504007, 2009.
- [56] H. Casini and M. Huerta. Reduced density matrix and internal dynamics for multicomponent regions. *Class. Quant. Grav.*, 26:185005, 2009.
- [57] Chang-Zhong Guo, Wen-Cong Gan, and Fu-Wen Shu. A note on the entanglement entropy of primary fermion fields in JT gravity*. *Chin. Phys. C*, 47(8):085106, 2023.
- [58] Bernard S. Kay and Robert M. Wald. Theorems on the uniqueness and thermal properties of stationary, nonsingular, quasifree states on spacetimes with a bifurcate killing horizon. *Physics Reports*, 207(2):49–136, 1991.
- [59] Paul Langlois. Hawking radiation for Dirac spinors on the RP^{*3} geon. *Phys. Rev. D*, 70:104008, 2004. [Erratum: Phys.Rev.D 72, 129902 (2005)].
- [60] Enrico Barausse and Thomas P. Sotiriou. Black holes in Lorentz-violating gravity theories. *Class. Quant. Grav.*, 30:244010, 2013.
- [61] Ted Jacobson and Aron C. Wall. Black Hole Thermodynamics and Lorentz Symmetry. *Found. Phys.*, 40:1076–1080, 2010.
- [62] D. Blas and S. Sibiryakov. Hořava gravity versus thermodynamics: The black hole case. *Phys. Rev. D*, 84:124043, Dec 2011.
- [63] V. Alan Kostelecký and Matthew Mewes. Fermions with lorentz-violating operators of arbitrary dimension. *Phys. Rev. D*, 88:096006, Nov 2013.
- [64] J. B. Hartle and S. W. Hawking. Path-integral derivation of black-hole radiance. *Phys. Rev. D*, 13:2188–2203, Apr 1976.
- [65] Matt Visser. Gravitational vacuum polarization. iii. energy conditions in the (1+1)-dimensional schwarzschild spacetime. *Phys. Rev. D*, 54:5123–5128, Oct 1996.
- [66] Claudio Dappiaggi, Valter Moretti, and Nicola Pinamonti. Rigorous construction and Hadamard property of the Unruh state in Schwarzschild spacetime. *Adv. Theor. Math. Phys.*, 15(2):355–447, 2011.
- [67] Edward Witten. APS Medal for Exceptional Achievement in Research: Invited article on entanglement properties of quantum field theory. *Rev. Mod. Phys.*, 90(4):045003, 2018.

- [68] Pasquale Calabrese and John Cardy. Entanglement entropy and conformal field theory. *J. Phys. A*, 42:504005, 2009.
- [69] Yoshinori Matsuo. Entanglement entropy and vacuum states in Schwarzschild geometry. *JHEP*, 06:109, 2022.
- [70] Yoshinori Matsuo. Islands and stretched horizon. *JHEP*, 07:051, 2021.
- [71] Pasquale Calabrese and John L. Cardy. Entanglement entropy and quantum field theory. *J. Stat. Mech.*, 0406:P06002, 2004.
- [72] Eugenio Bianchi, Tommaso De Lorenzo, and Matteo Smerlak. Entanglement entropy production in gravitational collapse: covariant regularization and solvable models. *JHEP*, 06:180, 2015.
- [73] Enrique Alvarez and Raquel Santos-Garcia. Cft in conformally flat spacetimes. *Phys. Rev. D*, 101:125009, Jun 2020.
- [74] H. Casini and M. Huerta. A Finite entanglement entropy and the c-theorem. *Phys. Lett. B*, 600:142–150, 2004.
- [75] H. Casini. Entropy localization and extensivity in the semiclassical black hole evaporation. *Phys. Rev. D*, 79:024015, Jan 2009.
- [76] H. Casini and M. Huerta. Remarks on the entanglement entropy for disconnected regions. *JHEP*, 03:048, 2009.
- [77] Pasquale Calabrese, John Cardy, and Erik Tonni. Entanglement entropy of two disjoint intervals in conformal field theory. *J. Stat. Mech.*, 0911:P11001, 2009.
- [78] Anirban Roy Chowdhury, Ashis Saha, and Sunandan Gangopadhyay. Role of mutual information in the page curve. *Phys. Rev. D*, 106:086019, Oct 2022.
- [79] Matthew Headrick. Lectures on entanglement entropy in field theory and holography. 7 2019.
- [80] Javier Molina-Vilaplana and Pasquale Sodano. Holographic View on Quantum Correlations and Mutual Information between Disjoint Blocks of a Quantum Critical System. *JHEP*, 10:011, 2011.
- [81] Pasquale Calabrese, John Cardy, and Erik Tonni. Entanglement negativity in extended systems: A field theoretical approach. *J. Stat. Mech.*, 1302:P02008, 2013.
- [82] Jonah Kudler-Flam and Shinsei Ryu. Entanglement negativity and minimal entanglement wedge cross sections in holographic theories. *Phys. Rev. D*, 99(10):106014, 2019.
- [83] Eduardo Martín-Martínez, T. Rick Perche, and Bruno de S. L. Torres. Broken covariance of particle detector models in relativistic quantum information. *Phys. Rev. D*, 103:025007, Jan 2021.
- [84] Dawei Wu, Shan-Chang Tang, and Yu Shi. Accelerating Unruh-DeWitt detectors coupled with a spinor field. *JHEP*, 06:190, 2023.
- [85] Franz Mandl and Graham Shaw. *QUANTUM FIELD THEORY*. 1985.
- [86] Daniel Hümmel, Eduardo Martín-Martínez, and Achim Kempf. Renormalized unruh-dewitt particle detector models for boson and fermion fields. *Phys. Rev. D*, 93:024019, Jan 2016.
- [87] Joseph I. Kapusta and Charles Gale. *Finite-Temperature Field Theory: Principles and Applications*. Cambridge Monographs on Mathematical Physics. Cambridge University Press, 2 edition, 2006.
- [88] W.G. Brenna, Robert B. Mann, and Eduardo Martín-Martínez. Anti-unruh phenomena. *Physics Letters B*, 757:307–311, 2016.
- [89] Luis C. Barbado, Carlos Barceló, Luis J. Garay, and Gil Jannes. Hawking versus Unruh effects, or the difficulty of slowly crossing a black hole horizon. *JHEP*, 10:161, 2016.

- [90] Luis C. Barbado, Carlos Barcelo, and Luis J. Garay. Hawking radiation as perceived by different observers: An analytic expression for the effective-temperature function. *Class. Quant. Grav.*, 29:075013, 2012.
- [91] Luis C. Barbado, Carlos Barcelo, and Luis J. Garay. Hawking radiation as perceived by different observers. *Class. Quant. Grav.*, 28:125021, 2011.
- [92] Sumanta Chakraborty, Suprit Singh, and T. Padmanabhan. A quantum peek inside the black hole event horizon. *JHEP*, 06:192, 2015.
- [93] Matteo Smerlak and Suprit Singh. New perspectives on Hawking radiation. *Phys. Rev. D*, 88(10):104023, 2013.
- [94] Grant Salton, Robert B. Mann, and Nicolas C. Menicucci. Acceleration-assisted entanglement harvesting and rangefinding. *New J. Phys.*, 17(3):035001, 2015.
- [95] Martin B. Plenio and Shashank S. Virmani. An Introduction to Entanglement Theory. *Quant. Inf. Comput.*, 7(1-2):001–051, 2007.
- [96] Alejandro Pozas-Kerstjens and Eduardo Martín-Martínez. Harvesting correlations from the quantum vacuum. *Phys. Rev. D*, 92:064042, Sep 2015.
- [97] F. Verstraete and J. I. Cirac. Continuous matrix product states for quantum fields. *Phys. Rev. Lett.*, 104:190405, May 2010.
- [98] Jutho Haegeman, Tobias J. Osborne, Henri Verschelde, and Frank Verstraete. Entanglement renormalization for quantum fields in real space. *Phys. Rev. Lett.*, 110:100402, Mar 2013.
- [99] Eduardo Martin-Martinez and Nicolas C. Menicucci. Entanglement in curved spacetimes and cosmology. *Class. Quant. Grav.*, 31(21):214001, 2014.
- [100] José de Ramón, Maria Papageorgiou, and Eduardo Martín-Martínez. Causality and signalling in noncompact detector-field interactions. *Phys. Rev. D*, 108:045015, Aug 2023.
- [101] Erickson Tjoa and Eduardo Martín-Martínez. When entanglement harvesting is not really harvesting. *Phys. Rev. D*, 104:125005, Dec 2021.
- [102] Matt Visser. Gravitational vacuum polarization. ii. energy conditions in the Boulware vacuum. *Phys. Rev. D*, 54:5116–5122, Oct 1996.
- [103] Keith K. Ng, Chen Zhang, Jorma Louko, and Robert B. Mann. A little excitement across the horizon. *New J. Phys.*, 24(10):103018, 2022.
- [104] Miguel Montero, Juan León, and Eduardo Martín-Martínez. Fermionic entanglement extinction in noninertial frames. *Phys. Rev. A*, 84:042320, Oct 2011.
- [105] S. Shankaranarayanan, K. Srinivasan, and T. Padmanabhan. Method of complex paths and general covariance of Hawking radiation. *Mod. Phys. Lett. A*, 16:571–578, 2001.
- [106] Ramit Dey, Stefano Liberati, Zahra Mirzaiyan, and Daniele Pranzetti. Black hole quantum atmosphere for freely falling observers. *Phys. Lett. B*, 797:134828, 2019.
- [107] George B. Arfken, Hans J. Weber, and Frank E. Harris. Chapter 12 - further topics in analysis. In George B. Arfken, Hans J. Weber, and Frank E. Harris, editors, *Mathematical Methods for Physicists (Seventh Edition)*, pages 551–598. Academic Press, Boston, seventh edition edition, 2013.